The present work proposes a simplified approach to model the thermo-mechanical coupling present in the SLM process. This model aims to obtain a qualitative description of the inufluence of some parameters in the distortion of the final part. The process is modelled as a quasi-static uncoupled thermo-mechanical problem, in a bidimensional domain, under the hypothesis of plain strain, temperature dependent thermal properties and updated Lagrangian description. The finite element method is used to solve the equilibrium equations. The laser source and the melting pool are modelled as a moving temperature field with prescribed temperature. The effect of both substrate preheating and scan strategy are studied and compared to results found in the literature.

Adviser: Eduardo Lenz Cardoso

Joinville, 2018

ANO
2018

SUELEN CRISTINA DA SILVA RIBEIRO | **A STUDY OF THERMO-MECHANICAL COUPLING IN THE SELECTIVE LASER MELTING PROCESS**

SANTA CATARINA STATE UNIVERSITY – UDESC
COLLEGE OF TECHNOLOGICAL SCIENCE – CCT
MECHANICAL ENGINEERING GRADUATE PROGRAM – PPGEM

MASTER THESIS

A STUDY OF THERMO-MECHANICAL COUPLING IN THE SELECTIVE LASER MELTING PROCESS

SUELEN CRISTINA DA SILVA RIBEIRO

JOINVILLE, 2018

SUELEN CRISTINA DA SILVA RIBEIRO

A STUDY OF THERMO-MECHANICAL COUPLING IN THE SELECTIVE LASER MELTING PROCESS

Master thesis submitted to the Mechanical Engineering Department at the College of Technological Science of Santa Catarina State University in fulfillment of the partial requirement for the Master's degree in Mechanical Engineering.

Adviser: Dr. Eduardo Lenz Cardoso

JOINVILLE - SC
2018

da Silva Ribeiro, Suelen Cristina
A study of Thermo-Mechanical coupling in the Selective Laser Melting Process / Suelen Cristina da Silva Ribeiro. - Joinville , 2018.
92 p.

Orientador: Eduardo Lenz Cardoso
Dissertação (Mestrado) - Universidade do Estado de Santa Catarina, Centro de Ciências Tecnológicas, Programa de Pós-Graduação em Engenharia Mecânica, Joinville, 2018.

1. Selective Laser Melting. 2. Thermo-Mechanical coupling. 3. Preheating. 4. Scan strategy. 5. Distortion. I. Lenz Cardoso, Eduardo. II. Universidade do Estado de Santa Catarina. Programa de Pós-Graduação. III. Título.

A STUDY OF THERMO-MECHANICAL COUPLING IN THE SELECTIVE LASER MELTING PROCESS

por

Suelen Cristina da Silva Ribeiro

Esta dissertação foi julgada adequada para obtenção do título de

MESTRA EM ENGENHARIA MECÂNICA

Área de concentração em "Modelagem e Simulação Numérica"
e aprovada em sua forma final pelo

CURSO DE MESTRADO ACADÊMICO EM ENGENHARIA MECÂNICA
DO CENTRO DE CIÊNCIAS TECNOLÓGICAS DA
UNIVERSIDADE DO ESTADO DE SANTA CATARINA.

Banca Examinadora:

Prof. Dr. Eduardo Lenz Cardoso
CCT/UDESC (Orientador/Presidente)

Prof. Dr. Tiago Vieira da Cunha
UFSC

Profa. Dra. Danielle Bond
CCT/UDESC

Joinville,SC, 29 de agosto de 2018.

ACKNOWLEDGMENTS

The author would like to express the following acknowledgements.

To Eduardo Lenz Cardoso, professor and advisor, for the support and all shared knowledge as well for the patience.

To the Santa Catarina State University for the high quality education provided.

To Professors and Professionals of the Mechanical Engineering Graduate Program that contributed for my formation.

To my parents, Salete e Aroldo, for the support, incentive, love and for providing the necessary and fundamental education that made all of it possible. I would like to thank you too for the valuable support to the care of my daughter Maria.

To my husband, Márcio, for the incentive, the emotional support and for believing in my capacity at every step.

To my sisters, Carolina and Fernanda, for the incentive and for the advices.

To my parents in law, Irene e Reinaldo, and my niece, Priscila (*in memoriam*), for the support to the care of my daughter.

To my daughter, Maria Cristina, for the wonderful moments of distraction.

To CAPES for the concession of the master's scholarship.

ABSTRACT

DA SILVA RIBEIRO, Suelen Cristina, A study of Thermo-Mechanical coupling in the Selective Laser Melting Process. 2018. Master Thesis (Master in Mechanical Engineering - Area: Numerical Modeling and Simulation) – Santa Catarina State University. Mechanical Engineering Graduate Program Joinville 2018.

The Additive Manufacturing (AM) process is a relatively new process used in many industrial sectors. The Selective Laser Melting (SLM) process is a kind of additive manufacturing where it is possible to print parts with complex geometries which would be hard to build using conventional processes. In the process a powder bed is melted by a fast moving laser beam, leading to fast solidification rates that incurs in residual stresses. After the manufacturing, the part is removed from the substrate and the residual stresses are then released, causing distortions and cracks in the final part. Since many parameters are involved in the SLM process, there are many possible combinations that can be used. Defining the best parameters to guarantee the quality of the part can be very costly when this process is purely experimental. In this way, a numerical formulation can helps in this task and can also be used to obtain the optimum set. Since the process involves very complex thermal and mechanical mechanisms, the present work proposes a simplified approach to model the thermo-mechanical coupling present in this process. This model aims to obtain a qualitative description of the influence of some parameters in the distortion of the final part. The process is modeled as a quasi-static uncoupled thermo-mechanical problem, in a bi dimensional domain, under the hypothesis of plane strain, temperature dependent thermal properties and updated Lagrangian description. The finite element method is used to solve the equilibrium equations. The laser source and the melting pool are modeled as a moving temperature field with prescribed temperature. The effect of both substrate preheating and scan strategy are studied and compared to results found in the literature. It is shown that the proposed formulation can describe the effect of substrate preheating on the distortion of the final part. Also, it is found that the use of temperature independent mechanical properties leads to a less sensitive prediction with respect to changes in this parameter. Among the many mechanisms associated to the effect of the scan strategy on the distortion of the final part, it is found that the proposed 2D formulation can properly predict the effect of local preheating.

Key-words: Selective Laser Melting, Thermo-Mechanical coupling, Preheating, Scan strategy, Distortion.

RESUMO

DA SILVA RIBEIRO, Suelen Cristina, A study of Thermo-Mechanical coupling in the Selective Laser Melting Process. 2018. Dissertação (Mestrado em Engenharia Mecânica - Área: Modelagem e Simulação Numérica) – Universidade do Estado de Santa Catarina. Programa de Pós-Graduação em Engenharia Mecânica Joinville 2018.

O processo de Manufatura Aditiva é um processo relativamente novo usado em muitos setores industriais. O processo de Fusão Seletiva a Laser (FSL) é um tipo de manufatura aditiva onde é possível imprimir peças com geometrias complexas que seriam economicamente inviáveis de construir usando processos convencionais. Nesse processo, um leito de pó é fundido por um feixe de laser que se movimenta rapidamente, levando à taxas de solidificação muito altas que introduzem tensões residuais. Após a fabricação, a peça é removida do substrato e as tensões residuais são então liberadas, causando distorções e trincas na peça final. Existem diversas combinações possiveis dos parâmetros do processo, e definir a melhor combinação para garantir a qualidade da peça pode ser muito custoso quando este processo é puramente experimental. Desta forma, uma formulação numérica pode ajudar nesta tarefa e também pode ser usada para obter o melhor conjunto de parâmetros. Como o processo envolve mecanismos térmicos e mecânicos muito complexos, o presente trabalho propõe uma abordagem simplificada para modelar o acoplamento termo-mecânico. Este modelo visa obter uma descrição qualitativa da influência de alguns parâmetros na distorção final da peça. O processo é modelado como um problema termomecânico semi-estático desacoplado, em um domínio bidimensional, sob a hipótese de estado plano de deformações, propriedades térmicas dependentes da temperatura e descrição Lagrangeana atualizada. A fonte de laser e a poça fundida são modeladas como um campo de temperatura móvel com temperatura prescrita. O efeito do pré-aquecimento do substrato e da estratégia de varredura do laser são estudados e comparados com os resultados encontrados na literatura. Mostra-se que a formulação proposta pode descrever o efeito do pré-aquecimento do substrato na distorção da peça. Além disso, verifica-se que o uso de propriedades mecânicas independentes da temperatura leva a uma predição de distorção menos sensível em relação à temperatura de pré-aquecimento do substrato. Verifica-se que a formulação 2D proposta pode prever adequadamente o efeito do pré-aquecimento local causado pela estratégia de varredura do laser utilizada.

Palavras-chave: Fusão Seletiva a Laser, Acoplamento Termo-Mecânico, Pré-aquecimento, Estratégia de varredura, Distorção.

Table of Contents

List of Figures

List of Tables

Chapter 1

Introduction

According to the ASTM-International (2015): "Additive Manufacturing (AM) is a process of joining materials to make parts from 3D model data, usually layer upon layer, as opposed to subtractive manufacturing and formative manufacturing methodologies". AM machines work in the same way: first they need a 3D computer-aided design (CAD) file with geometrical information about the part to be built; the 3D CAD is sliced into a stack of two-dimensional layers, that will be deposited one by one in order to build up the final part (STUCKER, 2012). Fig. 1.1 shows the original design and the corresponding sliced part.

Figure 1.1 – Example of sliced part to be built by the AM process

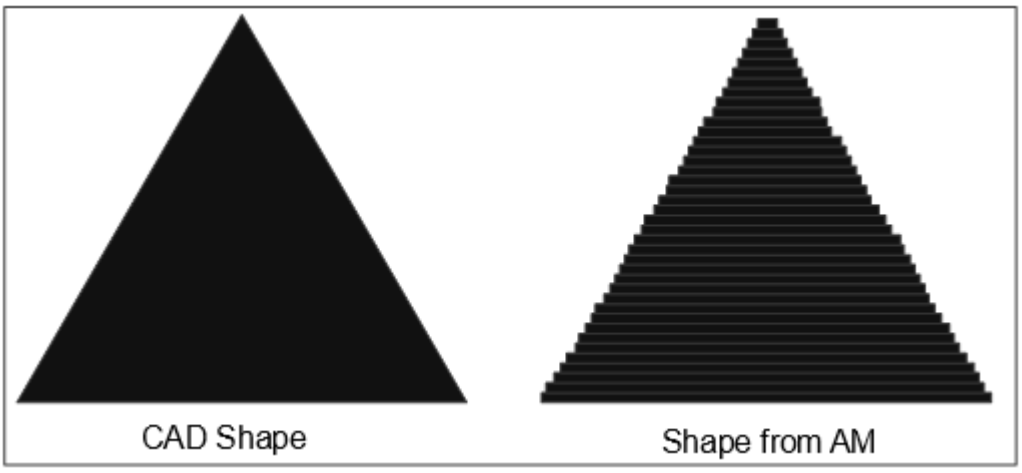

Source: Author's production based on Stucker (2012).

The basic concept of all AM processes is the same: adding material where it is needed. The difference among them is the base material, the way of supplying this material and the consolidation mechanism. ASTM-International (2015) defines seven categories of additive manufacturing:

- Binder jetting - *AM process where a liquid bonding agent is selectively deposited to join powder materials*;
- Directed energy deposition - *AM process in which focused thermal energy is used to fuse materials by melting as they are being deposited*;
- Material extrusion - *AM process in which material is selectively dispensed through a nozzle or an orifice*;
- Material jetting - *AM process in which droplets of base material are selectively deposited*;
- Powder bed fusion - *AM process in which thermal energy selectively fuses regions of a powder bed*;
- Sheet lamination - *AM process in which sheets of material are bonded to form an object*;
- Vat photopolymerization - *AM process in which liquid photopolymer in a vat is selectively cured by light-activated polymerization*.

Table 1.1 shows the technologies of each category and the material classes that can be processed by each one.

According to Vrancken (2016), Kusuma (2016) and Kempen (2015) the AM process has many advantages compared to conventional manufacturing process:

- It is more efficient since it uses less material to manufacture parts and has minimum material waste, hereby reducing lead times and costs;
- Although the process is slow, it is considered a fast manufacturing technique. Without using molds and dies, the AM technology allows the manufacturer to build prototypes and parts on demand, saving time during product design;
- The high geometrical freedom give the possibility to built complex parts, which are difficult or impossible to manufacture with traditional methods. For example, internal cavities, thin walls and lightweight structures.

According to Vrancken (2016) and Srivatsan et al. (2016) the AM process also has some limitations and disadvantages:

- The amount of base materials available to the AM process is limited, limiting the applicability of the AM process;
- The repeatability is not guaranteed in this process, such that every part needs to undergo quality control after the process. Therefore, if part quality could be guaranteed during the process, it would save both time and money;

Table 1.1 – Technologies of each category of AM process and material classes that can be processed.

AM Techniques	Technology	Material classes
Binder jetting	3D Printing Ink-jetting S-Print M-Print	Metal Polymer Ceramic
Directed energy deposition	Direct Metal Deposition Laser Deposition Laser Consolidation Electron Beam Direct Melting	Powder metal Wire metal
Material extrusion	Fused Deposition Modeling	Polymer
Material jetting	Polyjet Ink-jetting Thermojet	Photopolymer Wax
Powder bed fusion	Selective Laser Sintering Selective Laser Melting Electron Beam Melting	Polymer Metal Ceramic
Sheet lamination	Ultrasonic Consolidation Laminated Object Manufacturing	Hybrids Metalic Ceramic
Vat photopolymerization	Stereolithography Digital Light Processing	Photopolymer Ceramic

Source: Based on (CALIGNANO et al., 2017).

- The parts produced using additive manufacturing processes often have a rough and ribbed surface finish. This unfinished look requires further surface preparation by either machining or polishing;
- The AM process has a size limitation, where large objects become impractical when considering the large amount of time required to complete the build process;
- The initial cost of additive manufacturing equipment can be high;
- High cooling rates during the process create metastable, unique microstructures of which the mechanical behavior is not yet completely documented. Moreover, their response to heat treatment is different than the one found in cast or forged parts;
- Another effect of the high cooling rates are residual stresses, that can cause permanent deformations and can even lead to formation of cracks.

AM process plays an important role to build parts to many industrial sectors, like aerospace, automotive, biomedical, energy conversion, consumer products, engineered foods and sporting goods (SRIVATSAN et al., 2016). Fig. 1.2 shows some objects built by the AM process.

Figure 1.2 – Example of AM objects (a)Ring by Vulcan jewelry, (b) Purse from Kipling, (c) Bicycle seat and (d) Pendant light from Bathsheba Grossman.

Source: Adapted from Thompson et al. (2016).

The present work is focused in the powder bed fusion technique, in the Selective Laser Melting (SLM) technology. The SLM process produces components by selectively melting of a base powder material (powder bed) and is discussed in details in this work, but its worth to mention that the multiple modes of heat and mass transfer as well the chemical reactions that occur during the SLM process make it very complex to model. Although the process is widespread and applied in a variety of industrial sectors, the influence of the many possible parameters used to set up the process on the underlying thermal and stress fields are not fully understood (ROBERTS, 2012). The high thermal gradients present in the process lead to development of residual stresses in the manufactured part, leading to formation of micro-cracks and distortion. In this way, the parameters of the process must be combined to minimize the residual stresses in order to improve the manufactured part quality. A variety of experimental researches gives an idea of the influence of each parameter in the part produced by SLM process. However, each part has its peculiarities and what works for a specific part could not work properly for another. Therefore, it would be impracticable to make experimental tests for each part to be manufactured to find the best set.

Numerical algorithms are an efficient and widely applicable tool to model and predict the behavior of the part during the process. Besides allowing modelling the process, it is also supports process variable selection and further optimisation. The following chapters discuss the mechanisms involved and the need to properly model

the SLM process.

1.1 Objectives of Research

The main objective of this research is to develop a formulation to qualitatively predict the distortion behavior of parts produced by SLM process.

Two process parameters are evaluated: laser scan strategy and preheating temperature of the substrate. The aim is to verify the sensibility of the implemented model with respect to the parameters that have large influence in the final distortion of the part.

The process is modeled as a quasi-static uncoupled thermo-mechanical problem, in a bi dimensional domain, under the hypothesis of plane strain, temperature dependent thermal properties and updated Lagrangian description.

The laser source and the melting pool are modeled as a moving temperature field with prescribed temperature in order to simplify the model, since the local effect of the melting pool is neglected and only global behavior of the part is analyzed.

Thus, the main contributions of this work are the development of a simplified approach to model both the melting pool and the laser source as well as a detailed description of both the formulation and the underlying computer implementation.

Chapter 2

Selective Laser Melting

The Selective Laser Melting (SLM) is a powder bed fusion process created to produce components from powder (CALIGNANO et al., 2017) where a high intensity laser is used as energy source. The laser beam scans the loose powder, layer-by-layer, and through melt and solidification the part is built.

Many steps are involved from the beginning of the process to the final component. First a 3D CAD model is created with the desired shape of the component. Than a STL (Standard Tessellation Language) file is processed in order to create the necessary supports to any overhanging feature and to generate the sliced model in 2D cross sections. During the fabrication, a thin layer of powder is deposited on a substrate and the laser beam scans the layer according to 2D cross sections created before. Most of the energy from the laser is absorbed by the powder and, as a consequence, the temperature quickly rises up to the melting point, forming the melting pool. As soon as the laser beam leaves the melting pool, the metal is quickly solidified and the consolidated material starts to build the component (KUSUMA, 2016). When the scanning is completed, the building platform moves down and the dispenser platform moves up. The coater spread a new powder layer on top, and the laser scan this new layer. The laser scans the powder bed again and, layer-by-layer, the component is built. A controlled atmosphere is necessary inside the chamber during the fabrication due to the high temperatures involved in the melting process. Argon or nitrogen can be used as the inert gas to prevent oxidation and other problems (CALIGNANO et al., 2017). After the part is manufactured and cooled, the substrate is removed from the build chamber and the component is extracted, as well as the supports. Fig. 2.1 shows the schematic of a SLM machine.

Figure 2.1 – Schematic of a SLM machine

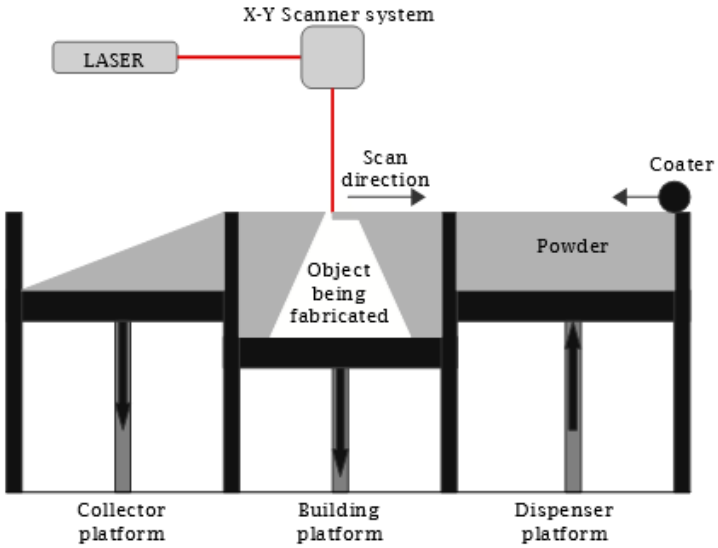

Source: Author's production based on (CALIGNANO et al., 2017)

Nowadays there are several alloys available for SLM process, including titanium, steel, aluminium, cobalt-chromium and nickel alloys (VRANCKEN, 2016), (CALIGNANO et al., 2017), (KRUTH et al., 2016). Some researches are being development with others kind of alloys, as for example, cooper, magnesium and precious metals (VRANCKEN, 2016). Titanium alloys are widely applied to built implants by the SLM process. Fig. 2.2 shows titanium implants for skull and pelvis.

Figure 2.2 – Titanium implants for skull (left) and pelvis (right)

Source: Thompson et al. (2016).

2.1 Process Parameters

In the SLM process, the final quality of the part is directly related to process parameters. Laser power, scan speed, scanning strategy, laser beam spot size, hatch spacing, layer thickness, powder properties and the temperature inside the chamber are the main parameters (KUSUMA, 2016). Fig. 2.3 shows the main parameters cited above.

Figure 2.3 – Main process parameters

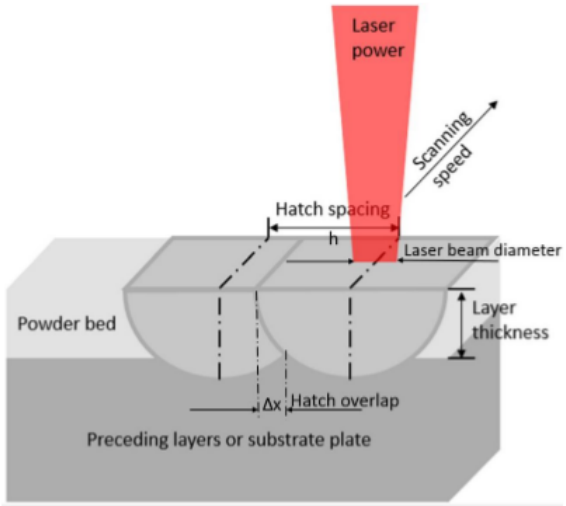

Source: (KUSUMA, 2016)

In the following, these parameters are presented:

- Laser power, scan speed, hatch spacing and layer thickness:

  These four parameters are often combined into a sigle parameter called volumetric energy density

$$E = \frac{P}{vht}[J/mm^3], \tag{2.1.1}$$

  where P is the laser power in $[W]$, v is the scan speed in $[mm/s]$, h is the hatch spacing in $[\mu m]$ and t is the layer thickness in $[\mu m]$ (VRANCKEN, 2016). The energy density is an engineering parameter representing the energy delivered to a unit volume of powder material (KRUTH et al., 2016) and can be useful to quickly compare parts made with different parameters (VRANCKEN, 2016).

- Scanning strategy:

  This parameter defines the way that each layer will be filled and has direct influence in the quality of the part (KEMPEN, 2015). Different scanning strategies

affect thermal history and consequently alter material properties, including density, residual stress and microstructure (KUSUMA, 2016) and (KRUTH et al., 2016). Fig. 2.4 shows the most common scan strategies.

Figure 2.4 – Scanning strategies: (A) unidirectional, (B) bidirectional, (C–F) alternating bidirectional (with different angles of 90^o, 60^o, 45^o, and 30^o), and (G) chessboard scanning strategy:

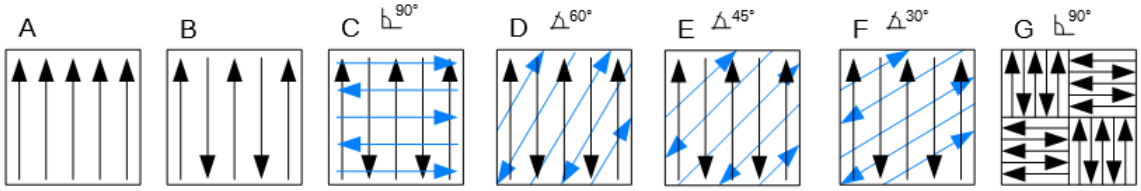

Source: Author's production based on (KRUTH et al., 2016)

The unidirectional strategy (Fig 2.4 A) is not frequently used, specially when the direction is not alternated in consecutive layers, because this tends to result in low material densities (VRANCKEN, 2016). Alternating the scan strategy in consecutive layers (Fig. 2.4 C-F) can improve the density (KEMPEN, 2015) and strongly affect the texture developed during the SLM process (VRANCKEN, 2016). A common scan strategy is the island scanning (Fig. 2.4 G) where the area to be filled is split into small square sectors, that are scanned sequentially. This subdivisions shortens the scan vectors, reducing residual stresses. To avoid aligned porosity, the consecutive layers can be rotated or shifted in order to change the island boundary position (VRANCKEN, 2016).

- Laser beam spot size:

  The width of the melting pool is mostly determined by the spot size, but also by the laser power and scan speed (VRANCKEN, 2016). The intensity I of the laser beam depends on the laser power and spot size (KEMPEN, 2015) and is defined as

$$I = \frac{4P}{\pi d^2}[W/mm^2]. \tag{2.1.2}$$

- Powder properties:

  The size of the powder grains plays an important role in SLM process due to the influence on the flowability (capacity to move by flow). The ratio of the larger to smaller particles can dictate the flowability, but humidity and particle shape can also affected this property (KUSUMA, 2016). To improve the flowability and the packing density the spherical shape is preferable. The packing density can also

be improved by using very small particles. The upper bound of the grains size is the layer thickness (KEMPEN, 2015).

- Ambient Temperature:

  The temperature inside the chamber, and thus the preheating of the powder and substrate, has strong influence on the process (ELSEN, 2007). Generally, higher temperatures are better for the process, and it should be uniformly distributed (KUSUMA, 2016). In a high ambient temperature, thermal gradients are lower and less energy is needed to fully melt the powder (KEMPEN, 2015). (ELSEN, 2007).

- Atmosphere:

  The atmosphere inside the chamber is the first parameter to be controlled in the SLM process, since non-inert particles, like oxygen, can react with the melting pool (ELSEN, 2007). An inert gas must be used, like argon or nitrogen, to prevent oxidation and other problems that impact the mechanical properties of the part (CALIGNANO et al., 2017).

2.2 Thermal Behavior on the SLM Process

The energy from the laser is transferred by four major mechanisms: reflection, conduction, convection and radiation. In the case of metallic powders, a large part of incident energy is reflected and the absorptivity depends on the material and powder morphology. The absorbed energy is partially conducted through the powder bed, solidified material and substrate, while part of the energy is lost by convection to the chamber's atmosphere and due to radiation (ZENG et al., 2015). Coupled heat transfer mechanisms make the thermal behavior during the SLM process very complex (YUAN; GU, 2015). Fig. 2.5 shows the heat transfer mechanisms present in the SLM process.

Significant radiation losses would occur at temperature above $1000K$, but the effect of radiation heat loss is usually assumed to be negligible for spot sizes smaller than 1.0 mm, according to Vasudevan Raghavan et al. (2008), apud (SHUAI et al., 2013).

During the SLM process, both high laser speed and power lead to fast heating and melting, forming the melting pool, followed by fast solidification. The size and shape of the melting pool, as well as the cooling rate and phase transformations, are strongly affected by its resultant fluid flow and heat transfer (KRUTH et al., 2016). The complexity of the mechanisms involved in the melting pool turn it very complex to properly model.

There are several problems that can occur in the melting pool due to bad combination of process parameters. A combination of low power and high scan speed can not delivery enough energy to fully melt the powder. On the other hand, when the scan

Figure 2.5 – Schematic of heat transfer mechanisms in SLM process

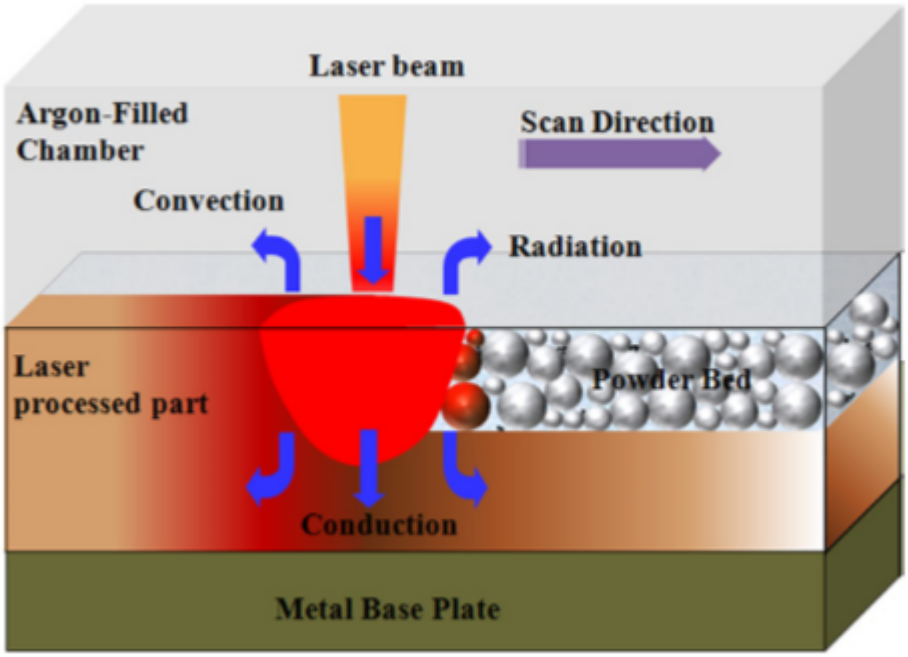

Source: (YUAN; GU, 2015)

speed is high and the power is sufficiently high to fully melt the powder, the balling phenomena can occur due to the break up of the elongated melting pool into smaller melts droplets (VRANCKEN, 2016). The keyhole mode regime takes place when the power is high and the scan speed is low, since an excess of energy is delivered to the material. In this regime, the melt penetrates deep into the material due its vaporization (KEMPEN, 2015). Fig. 2.6 shows the different melting regimes when varying the laser power and scan speed. The conduction zone is where a good part density is achieved.

A widely adopted model to describe the spatial distribution of heat source from the laser beam is the Gaussian distribution, leading to a symmetric distribution of laser irradiance across the beam, as depicted in Fig. 2.7. The input heat flux is defined as

$$q_{laser} = \frac{2AP}{\pi\omega^2} exp\left(-\frac{2r^2}{\omega^2}\right) [W/m^2], \tag{2.2.3}$$

where A is the absorption rate of powder material, P is the laser power, ω is the laser spot radius and r is the distance from the center of the laser beam to a point on the surface of the powder bed (YUAN; GU, 2015). Fig. 2.7 shows the Gaussian distribution, where its possible to see that further points receive less energy than points near to the center. The heat flux magnitude increases from $78.43[GW/m^2]$ to $156.86[GW/m^2]$ when the laser power rises from $100[W]$ to $200[W]$.

Figure 2.6 – Process window

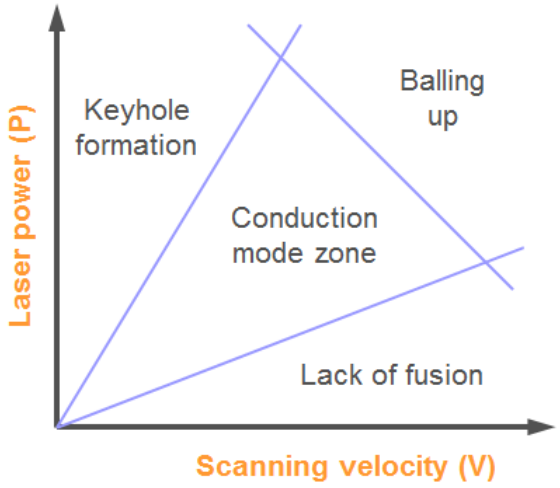

Source: (SAUNDERS, 2017.)

Figure 2.7 – Gaussian distribution of the laser beam with $\omega = 25[\mu m]$, powder absorption $A = 0.77$, $P = 100[W]$, $P = 150[W]$ and $P = 200[W]$.

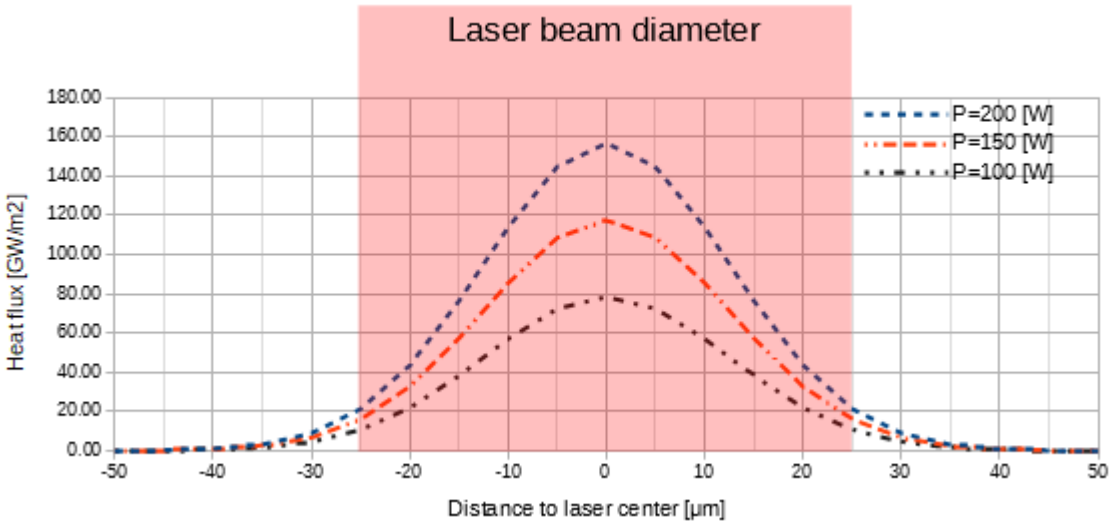

Source: Author's production

2.3 Residual Stresses on the SLM Process

Due to both high heating and cooling rates and quick scanning speed, the SLM process involves large thermal gradients (ALVAREZ et al., 2016). These large thermal gradients induce thermal expansion of the material, but it may not freely expand due

to constraints (substrate and previously solidified layers) (WU et al., 2017). In this way, residual stress are caused in the manufactured part leading to distortions and, in extreme cases, formation of micro-cracks (MATSUMOTO et al., 2002).

Residual stress are stresses that remain in a part when it reaches equilibrium with its environment. It can be defined based on the scale over which they self equilibrate. Type I residual stress act on the whole body and would cause a deformation of the body if boundary conditions are changed. This kind of residual stress is distributed over the entire structure and is also known as macroscopic residual stress. Type II and Type III residual stresses occur due to different material phases and due to dislocations at atomic scale, respectively. They are also known as microscopic residual stress (MERCELIS; KRUTH, 2006) and (VRANCKEN, 2016).

In the SLM process, Type I residual stresses are caused by two mechanisms. The first one is the Temperature Gradient Mechanism (TGM) resulting from the large thermal gradient that occurs around the laser spot. The upper layers tend to expand due to the high temperatures, but this expansion is constrained by the underlying solidified layers, such that a compressive stress is induced at the top. With high temperatures, the yield strength decreases and when it is reached, the compressive stresses in the material cause plastic deformation of the upper layers. When the upper layers cool down, the compressive state is converted into residual tensile stresses. Fig. 2.8 shows the TGM mechanism. In the second phenomenon, the melted top layers tend to shrink due to the thermal contraction. This deformation is again hindered by the underlying layers, thus introducing tensile stresses in the top layer, and compressive stresses below (KEMPEN et al., 2013) and (MERCELIS; KRUTH, 2006).

Figure 2.8 – TGM mechanism in SLM process

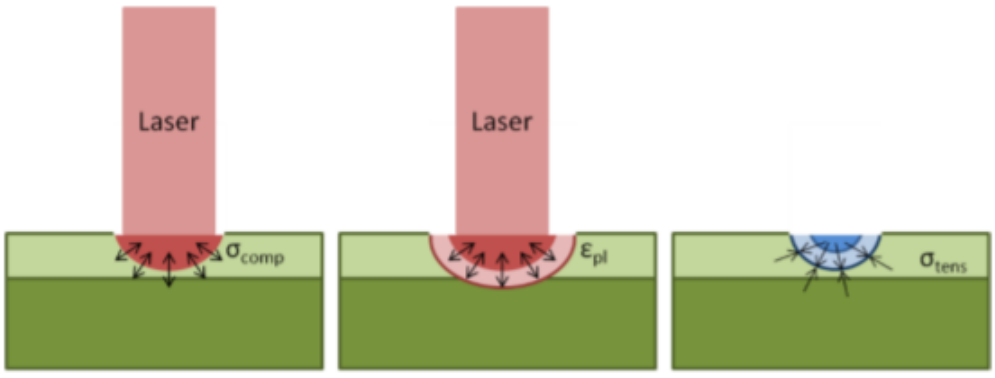

Source: (KEMPEN et al., 2013)

Scan strategy and substrate preheating are the main process parameters that can impact on deformations and residual stress (ZAEH; BRANNER, 2010). Several au-

thors found that the deformation of the part was larger in the direction of the scan tracks, such that, limiting the length of the scan vector can reduce part distortion (VRANCKEN, 2016). Nickel et al. (1999) investigated two different deposition patterns on a beam substrate: a long raster pattern (2.9 a) and a short raster pattern (2.9 b). They concluded that the long raster pattern leads to larger distortions when compared to the short raster pattern (2.9 c) by comparing experimental tests with numerical results.

Figure 2.9 – Investigation of two different deposition patterns. a) Long Raster Pattern. b) Short Raster Pattern. c) Beam Deflection.

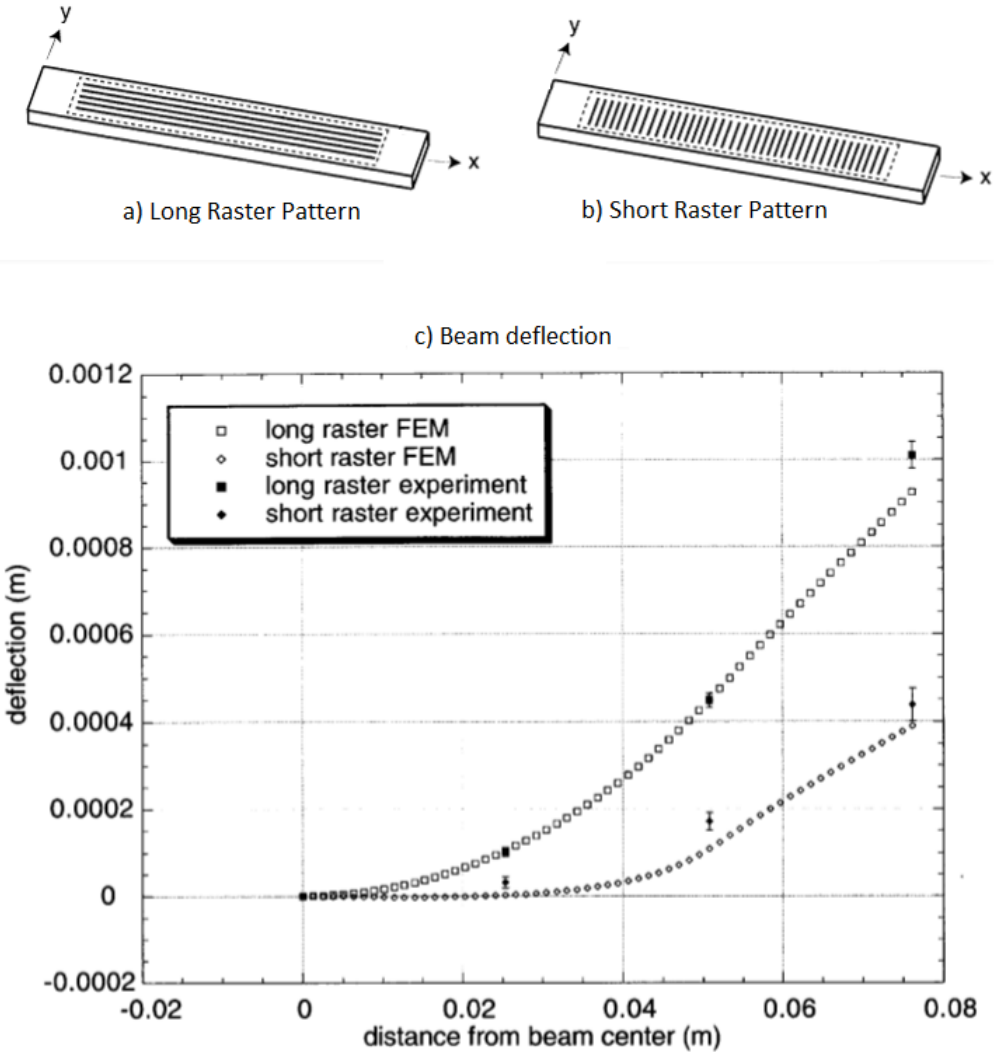

Source: (NICKEL et al., 1999)

The substrate preheating lead to decreasing temperature gradients, which also decreases residual stress (VRANCKEN, 2016). Bremen et al. (2012) studied this effect on the final distortion of twin cantilever beams. Five temperatures were studied (no preheating, 100, 150, 200 and 250 $^{\circ}C$). The results, Fig. 2.10, show that preheating

temperature has a large impact on final distortion of the part, since the deflection of the beam decreasing from $3[mm]$ to $0[mm]$ when the temperature is increased.

Figure 2.10 – Preheating of substrate to avoid distortion of twin cantilever made with aluminium alloy AlSi10Mg

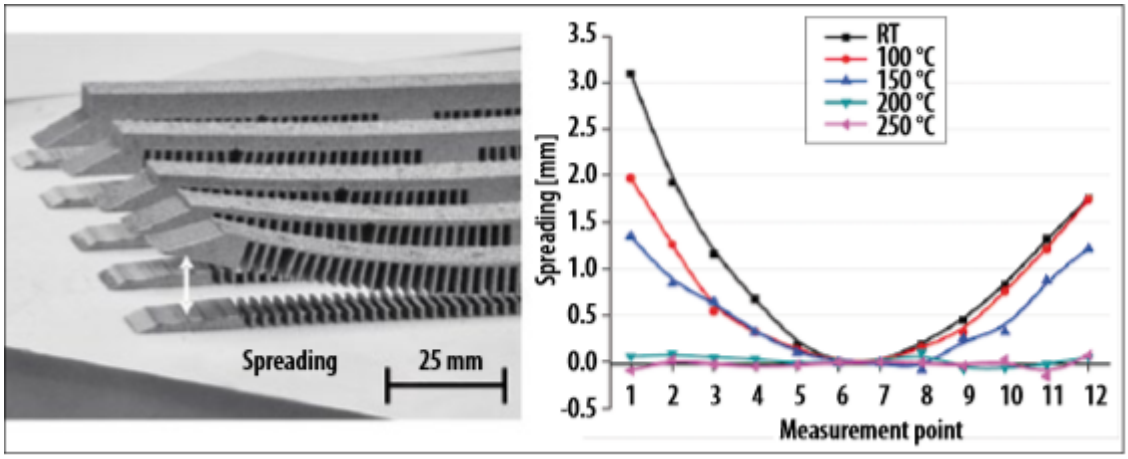

Source: (BREMEN et al., 2012)

Chapter 3

Heat Transfer Formulation

The energy balance equation is

$$\dot{E}_{in} + \dot{E}_g = \dot{E}_{out} + \dot{E}_{ie}, \tag{3.0.1}$$

where $\dot{E}_{in}$ is the rate of energy inflow, $\dot{E}_g$ is the rate of energy generated inside the system, $\dot{E}_{out}$ is the rate of energy outflow and $\dot{E}_{ie}$ is the rate change in enthalpy (RAO, 2004).

Consider a differential element with volume $dxdydz$, as shown in Fig. 3.1. The energy balance given by Eq. (3.0.1) can be written as

$$(q_x dydz + q_y dxdz + q_z dxdy) + \dot{Q}dxdydz = (q_{x+dx}dydz + q_{y+dy}dxdz + q_{z+dz}dxdy) + \dot{H}dxdydz, \tag{3.0.2}$$

where $\dot{Q}[W/m^3]$ is a volumetric heat source, $\dot{H}[W/m^3]$ is the rate of enthalpy,

$$q_i = -k_{ij}\frac{\partial T}{\partial j}, i, j = x, y, z, \tag{3.0.3}$$

are heat fluxes and $k_{ij}[W/mK]$ is the thermal conductivity tensor of the material.

Assuming an infinitesimal volume, q_{i+di} can be written as

$$q_{i+di} \approx q_i + \frac{\partial q_i}{\partial i}di, i = x, y, z, \tag{3.0.4}$$

such that Eq. (3.0.2) results in

$$\dot{Q} = \frac{\partial q_x}{\partial x} + \frac{\partial q_y}{\partial y} + \frac{\partial q_z}{\partial z} + \dot{H}, \tag{3.0.5}$$

after dividing each term by $dxdydz$.

Assuming an isotropic medium and substituting Eq. (3.0.3) in Eq. (3.0.5) we

Figure 3.1 – Heat fluxes in a differential volume element with volume $dxdydz$

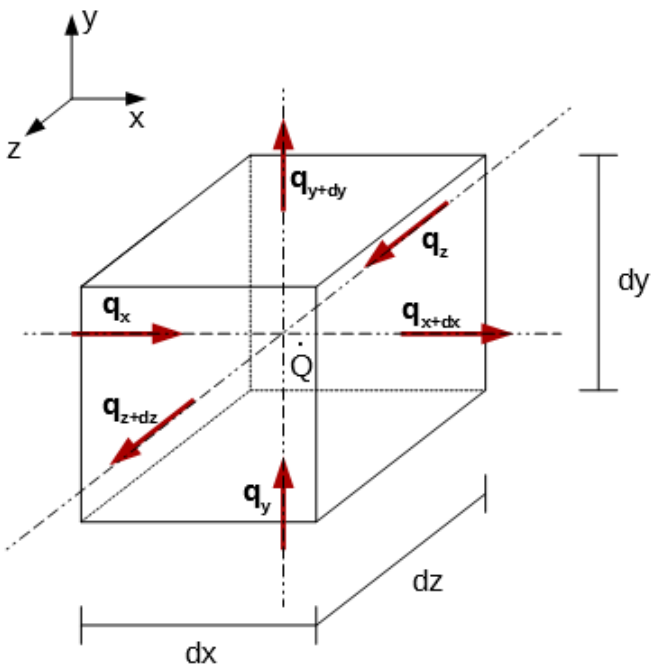

Source: Author's production

obtain

$$\dot{Q} = \frac{\partial}{\partial x}\left(-k_x \frac{\partial T}{\partial x}\right) + \frac{\partial}{\partial y}\left(-k_y \frac{\partial T}{\partial y}\right) + \frac{\partial}{\partial z}\left(-k_z \frac{\partial T}{\partial z}\right) + \dot{H} \tag{3.0.6}$$

or, in compact notation,

$$\dot{H} = \nabla \cdot (\mathbf{k}\nabla T) + \dot{Q}. \tag{3.0.7}$$

The boundary conditions can be either prescribed temperatures

$$T(x, y, z, t) = T_S \quad on \quad S^T, \tag{3.0.8}$$

where T_S is the known surface temperature on S^T, or prescribed heat flux

$$-k_n \frac{\partial T}{\partial n}\bigg|_{S^q} = q_s + h(T - T_a) + \sigma\varepsilon(T^4 - T_a^4), \tag{3.0.9}$$

where q_s is the prescribed heat flux, $h[W/m^2K]$ is the heat transfer coefficient, $\sigma[W/m^2K^4]$ is the Stefan-Boltzmann constant, ε is the emissivity of the surface, n denotes the normal axis to the surface S^q, T is the unknown surface temperature and T_a is the known ambient temperature. The second term of Eq. (3.0.9) is due to convection boundary condition and the third is due to radiation boundary condition.

For transient problems it is necessary to specify an initial temperature field at time $t = 0$,

$$T(x, y, z, 0) = T_0(x, y, z). \tag{3.0.10}$$

In the case of substrate preheating, initial temperature is T_{ph} (temperature of preheating).

Pal et al. (2016) and Zeng et al. (2015) used a fixed thermal boundary condition at the bottom of the substrate, since the temperature is assumed as constant during the process

$$T(x, y, z = 0, t) = T_{fixed} \, \forall t, \tag{3.0.11}$$

where T_{fixed} is the fixed temperature at the base of substrate ($z = 0$).

3.1 Stefan's Problem

The enthalpy time rate $\dot{H}$ can be written as

$$\dot{H} = \frac{\partial H}{\partial T}\frac{\partial T}{\partial t}, \tag{3.1.12}$$

and, for a problem without phase change,

$$\frac{\partial H}{\partial T} = \rho c, \tag{3.1.13}$$

where $\rho[kg/m^3]$ is the the density and $c[J/kgK]$ is the specific heat. In such case Eq. (3.1.12) becomes

$$\dot{H} = \rho c \frac{\partial T}{\partial t}. \tag{3.1.14}$$

However when the problem involves phase change (Stefan's Problem) it is characterized by a moving phase change boundary at which a heat balance condition must be taken into account. The domain consists of a solid region and a liquid region separated by an interface $\Gamma(t)$, which is at the phase change temperature T_m (VOLLER, 1997). Heat transfer in the solid region is described by

$$\rho c_s \frac{\partial T_s}{\partial t} = \nabla \cdot (\mathbf{k}_s \nabla T_s), \tag{3.1.15}$$

and, in the liquid region, by

$$\rho c_l \frac{\partial T_l}{\partial t} = \nabla \cdot (\mathbf{k}_l \nabla T_l). \tag{3.1.16}$$

The Stefan condition at the solid/liquid moving interface is

$$\mathbf{k}_s \nabla T_s \cdot \mathbf{n} - \mathbf{k}_l \nabla T_l \cdot \mathbf{n} = \rho L \mathbf{v} \cdot \mathbf{n}, \tag{3.1.17}$$

where $\mathbf{n}$ is the unit normal to the interface, $\mathbf{v}$ is the velocity of the interface and L is the latent heat in $[J/kg]$.

This problem can be solved in many ways, where fixed grid schemes or deforming grid/front tracking schemes can be used and the variable can be either nodal temperatures T or enthalpy H. Voller (1997) and Idelsohn et al. (1994) discussed various methods that can be used. Among them, the apparent heat capacity method is employed in this work. This approach absorbs the non-linear behavior associated with the phase change into the definition of a lumped heat capacity c_A

$$c_A = \begin{cases} c_s & \text{if } T \leq T_s \\ \frac{L}{T_l - T_s} + c_l & \text{if } T_s < T < T_l \\ c_l & \text{if } T \geq T_l \end{cases} . \tag{3.1.18}$$

were c_l is the liquid specific heat, c_s is the solid specific heat, T_s is the solidus temperature and T_l is the liquidus temperature (OGOH; GROULX, 2010).

The governing equation than becomes

$$\rho c_A \frac{\partial T}{\partial t} = \nabla \cdot (\mathbf{k} \nabla T) \tag{3.1.19}$$

such that the same equation is used through the simulation.

3.2 Finite Element Discretization

Using the weighted residuals method, we can rewrite Eq. (3.0.7) as

$$\int_V w \left(\rho c \frac{\partial T}{\partial t} - \nabla \cdot (\mathbf{k} \nabla T) - \dot{Q} \right) dV = 0, \tag{3.2.20}$$

or

$$\int_V w \nabla \cdot (\mathbf{k} \nabla T) dV + \int_V w \dot{Q} dV = \int_V w \rho c \frac{\partial T}{\partial t} dV, \tag{3.2.21}$$

where w is the test (or weight) function and V is the domain.

Applying Green's First identity to the first term, we obtain

$$\int_S w \mathbf{k} \frac{\partial T}{\partial n} dS - \int_V \nabla w \mathbf{k} \nabla T dV + \int_V w \dot{Q} dV = \int_V w \rho c \frac{\partial T}{\partial t} dV \tag{3.2.22}$$

where $\mathbf{n}$ is the outer normal to the surface and S is the surface. Neglecting radiation

effects, the first term can be split according to Eq. (3.0.9), resulting in

$$-\int_{S_1} wq_S dS_1 - \int_{S_2} wh(T - T_a)dS_2 \tag{3.2.23}$$
$$-\int_V \nabla w \cdot (\mathbf{k}\nabla T)\, dV + \int_V w\dot{Q}dV = \int_V w\rho c\frac{\partial T}{\partial t}dV$$

where S_1 and S_2 are the surfaces with prescribed heat flow.

Domain V is divided into E finite elements of p nodes and volume V_e. The temperature inside a finite element can be approximated as

$$T(x, y, z) = \mathbf{NT}, \tag{3.2.24}$$

with

$$\mathbf{N} = [\ N_1 \quad \dots \quad N_p\ ] \tag{3.2.25}$$

where N_i are the shape functions used for temperature interpolation inside a finite element and

$$\mathbf{T} = [\ T_1 \quad \dots \quad T_p\ ]^T, \tag{3.2.26}$$

where T_i are the nodal temperatures.

The thermal gradient can be written as

$$\nabla T = \nabla(\boldsymbol{NT}) = \nabla(\boldsymbol{N})\boldsymbol{T} \tag{3.2.27}$$

such that

$$\nabla(\boldsymbol{N})\boldsymbol{T} = \begin{bmatrix} \partial N_1/\partial x & \dots & \partial N_p/\partial x \\ \partial N_1/\partial y & \dots & \partial N_p/\partial y \\ \partial N_1/\partial z & \dots & \partial N_p/\partial z \end{bmatrix} \mathbf{T} = \mathbf{BT} \tag{3.2.28}$$

where $\mathbf{B}$ is the matrix for thermal gradients interpolation.

We assumed that the weighting function w follows the same interpolation of temperature,

$$\mathbf{w} = \mathbf{NW} \tag{3.2.29}$$

where $\mathbf{W}$ is a vector with nodal values of w. Substituting Eqs. (3.2.24), (3.2.28) and

(3.2.29) in Eq. (3.2.24) we obtain

$$\boldsymbol{W}^T \int_{V_e} \mathbf{N}^T \rho c \mathbf{N} dV \dot{\mathbf{T}} + \boldsymbol{W}^T \int_{V_e} \mathbf{B}^T \mathbf{k} \mathbf{B} dV \mathbf{T} + \boldsymbol{W}^T \int_{S_2} h \mathbf{N}^T \mathbf{N} dS_2 \mathbf{T} = \tag{3.2.30}$$
$$\boldsymbol{W}^T \int_{V_e} \dot{Q} \mathbf{N}^T dV - \boldsymbol{W}^T \int_{S_1} q_S \mathbf{N}^T dS_1 + \boldsymbol{W}^T \int_{S_2} h T_a \mathbf{N}^T dS_2$$

for each finite element.

After assembling the influence of each element in the finite element mesh we obtain

$$\mathbf{C_T} \dot{\mathbf{T}} + \mathbf{K_T} \mathbf{T} = \mathbf{F_T} \tag{3.2.31}$$

where

$$\mathbf{C_T} = \bigcup_{e=1}^{E} \int_{V_e} \mathbf{N}^T \rho c \mathbf{N} dV, \tag{3.2.32}$$

$$\mathbf{K_T} = \mathbf{K_c} + \mathbf{K_h} \tag{3.2.33}$$

where

$$\mathbf{K_c} = \bigcup_{e=1}^{E} \int_{V_e} \mathbf{B}^T \mathbf{k} \mathbf{B} dV, \tag{3.2.34}$$

$$\mathbf{K_h} = \bigcup_{e=1}^{E} \int_{S_2} h \mathbf{N}^T \mathbf{N} dS, \tag{3.2.35}$$

and

$$\mathbf{F_T} = \mathbf{F_{\dot{q}}} + \mathbf{F_{qs}} + \mathbf{F_h} \tag{3.2.36}$$

where

$$\mathbf{F_{\dot{Q}}} = \bigcup_{e=1}^{E} \int_{V_e} \dot{q} \mathbf{N}^T dV, \tag{3.2.37}$$

$$\mathbf{F_{qs}} = -\bigcup_{e=1}^{E} \int_{S_1} q_S \mathbf{N}^T dS, \tag{3.2.38}$$

$$\mathbf{F_h} = \bigcup_{e=1}^{E} \int_{S_2} h T_a \mathbf{N}^T dS. \tag{3.2.39}$$

3.3 Time Discretization

Recall Eq. (3.2.31)

$$\mathbf{C_T} \dot{\mathbf{T}} + \mathbf{K_T} \mathbf{T} = \mathbf{F_T},$$

where $\mathbf{C}_T$ is the capacity matrix, $\mathbf{K}_T$ is the conductivity matrix, $\mathbf{F}_T$ is the heat supply vector, $\mathbf{T}$ is the temperature vector and $\dot{\mathbf{T}}$ is the time derivative of $\mathbf{T}$.

The heat supply is a prescribed function of t and can be writen as $\mathbf{F}_T = \mathbf{F}_T(t)$

for $t \in [0, t_f]$. $\mathbf{C}_T$ is positive-definite and $\mathbf{K}_T$ is usually positive-definite (HUGHES, 2000).

Consider two temperature states $\mathbf{T}_n$ and $\mathbf{T}_{n+1}$, separated by a time increment Δt: the generalized trapezoidal rule is a temporal integration scheme based on the assumption that two subsequent temperature states follow

$$\mathbf{T}_{n+1} = \mathbf{T}_n + [(1 - \alpha_N)\dot{\mathbf{T}}_n + \alpha_N \dot{\mathbf{T}}_{n+1}]\Delta t, \tag{3.3.40}$$

where $\alpha_N \in [0, 1]$ (COOK et al., 1989). Different values of α_N lead to different methods, with different properties (Tab. 3.1).

Table 3.1 – Generalized trapezoidal methods

α_N	Method
0	Forward difference; forward Euler
$1/2$	Trapezoidal rule; Crank-Nicolson
$2/3$	Galerkin
1	Backward difference

Source: (COOK et al., 1989).

The stability of the algorithm depends on α_N. If $\alpha_N \geq 1/2$, the algorithm is unconditionally stable, such that there is no time step constraint. If $\alpha_N < 1/2$, the algorithm is conditionally stable and the largest Δt for stability, in the case of constant thermal properties, is (HUGHES, 2000)

$$\Delta t_{cr} = \frac{2}{(1 - 2\alpha_N)\lambda_{max}}, \tag{3.3.41}$$

where λ_{max} is the largest eigenvalue of

$$[\mathbf{K_T} - \lambda \mathbf{C_T}]\mathbf{T} = \mathbf{0}. \tag{3.3.42}$$

Given $\mathbf{T}_n$ and $\dot{\mathbf{T}}_n$ it is possible to find $\mathbf{T}_{n+1}$ and $\dot{\mathbf{T}}_{n+1}$. The procedure begins at $n = 0$ with $\mathbf{T}_0$ known. The initial value $\dot{\mathbf{T}}_0$ may be found from Eq. (3.2.31) at time $t = 0$

$$\mathbf{C_T}\dot{\mathbf{T}}_0 = \mathbf{F_{T0}} - \mathbf{K_T}\mathbf{T}_0. \tag{3.3.43}$$

If $\alpha_N = 0$, the algorithm is explicit, otherwise it is implicit. If $\mathbf{C_T}$ is a diagonal matrix and $\alpha_N = 0$, the computational effort per time step is small, as well as the Δt_{cr} (COOK et al., 1989).

As mentioned before, high speeds are involved in the SLM process and very small time steps are needed to properly model its behavior. Large temperature ranges are also involved in the process, and thermal properties, as thermal conductivity $\mathbf{k}$ and

specific heat c, depend on temperature. Therefore, in order to model the non-linear behavior of the thermal properties as a linear problem, small time steps are needed. The Forward difference ($\alpha_N = 0$) and a diagonal capacity matrix are used in order to reduce computational efforts and due to the quickness of the phenomena intrinsic to the process.

A special lumping technique was employed to determine the capacity matrix $\mathbf{C_T}$. This technique always produces positive lumped masses due to proportionality to the diagonal of the consistent matrix, that is always positive (HUGHES, 2000)

$$C_{ii}{}^{e} = \beta \int_{V_e} \rho c N_i^2 dV, i = 1 \dots nnodes, \tag{3.3.44}$$

were $nnodes$ is the total number of nodes in the element and β is

$$\beta = \frac{\int_{V_e} \rho c dV}{\sum_{i=1}^{nnodes} \int_{V_e} \rho c N_i^2 dV} = \frac{\text{Total element capacity}}{\text{Trace of consistent matrix}}. \tag{3.3.45}$$

With $\alpha_N = 0$, Eq. (3.3.40) becomes

$$\mathbf{T}_{n+1} = \mathbf{T}_n + \dot{\mathbf{T}}_n \Delta t, \tag{3.3.46}$$

and with a diagonal $\mathbf{C_T}$, the time stepping procedure becomes

- Step 1: Given the i-th nodal temperature at iteration n, T_i^n,
  evaluate $\mathbf{P} = \mathbf{K}_T^n \mathbf{T}^n$ and find $\dot{T_i^n} = \frac{1}{C_{ii}^n} \left(F_i^n - P_i\right)$
- Step 2: Find $T_i^{n+1} = T_i^n + \Delta t \dot{T_i^n}$.
- Step 3: Prescribe nodal temperatures $T_j^{n+1} = T_{Prescribed}$ and return to step 1.

Chapter 4

Thermo-Mechanical Formulation

As mentioned in the previous section, residual stresses can lead to formation of micro-cracks and distortion of the manufactured part. In this way, a proper modelling of the thermoelastic behavior is needed to predict the stress state of the part as well as the distortions. In the present formulation, only Type I residual stresses are taken into account.

According to Oden (1969), there are different approaches to model thermoelastic problems: static uncoupled, quasi-static uncoupled, dynamical uncoupled and coupled. The static uncoupled thermoelastic problem is considered to be two disjoint problems: The steady-state heat conduction problem in a rigid body and the problem of static deformation of an elastic solid subjected to steady, prescribed temperature distributions. The temperature field obtained from the first problem is the input of the second problem. The quasi-static uncoupled problem is a more general theory where the results from a transient heat conduction problem are used as input to a series of static elastic problems. If inertia terms are considered in the equations of motion, it becomes the dynamical theory of uncoupled thermoelasticity. The problem becomes a problem of coupled thermoelasticity when the deformation of the body is accounted for in the heat conduction equation and the influence of changes in temperature appears in the equations of motion. In this work, the SLM process is considered as a quasi-static uncoupled problem.

4.1 Equilibrium formulation

The movement of a body can be commonly described by two approaches: spatial (Eulerian Formulation) and material (Lagrangian Formulation). The material approach is used in this work, in particular, the Updated Lagrangian approach, where the equilibrium equations are written with respect to the last equilibrium configuration.

The equilibrium at configuration $t + \Delta t$, can be modeled by using the principle

of virtual displacements

$$\int_{^{t+\Delta t}V} {}^{t+\Delta t}\sigma_{ij}\delta^{t+\Delta t}e_{ij}d^{t+\Delta t}V = {}^{t+\Delta t}W, \tag{4.1.1}$$

where ${}^{t+\Delta t}\sigma_{ij}$ is the Cauchy stress tensor in the deformed geometry, $\delta^{t+\Delta t}e_{ij}$ is the infinitesimal virtual strain tensor

$$\delta^{t+\Delta t}e_{ij} = \frac{1}{2}\left(\frac{\partial\delta u_i}{\partial^{t+\Delta t}x_j} + \frac{\partial\delta u_j}{\partial^{t+\Delta t}x_i}\right), \tag{4.1.2}$$

where δu_i are the components of virtual displacement vector at $t+\Delta t$ with respect to t, ${}^{t+\Delta t}x_j$ are the Cartesian coordinates of material point at $t+\Delta t$, ${}^{t+\Delta t}V$ is the volume at $t+\Delta t$ and ${}^{t+\Delta t}W$ is

$${}^{t+\Delta t}W = \int_{^{t+\Delta t}V} {}^{t+\Delta t}f_i^B\delta u_i d^{t+\Delta t}V + \int_{^{t+\Delta t}S_f} {}^{t+\Delta t}f_i^S\delta u_i^S d^{t+\Delta t}S, \tag{4.1.3}$$

where ${}^{t+\Delta t}f_i^B$ are the components of body forces per unit volume at $t+\Delta t$, ${}^{t+\Delta t}f_i^S$ are the components of externally applied surface tractions per unit surface area at $t+\Delta t$, ${}^{t+\Delta t}S_f$ is the surface at $t+\Delta t$ on which external tractions are applied and δu_i^S is δu_i evaluated on the surface ${}^{t+\Delta t}S_f$. Fig. 4.1 shows a body subjected to a virtual displacement.

Since the second Piola-Kirchhoff stress tensor (${}_t^{t+\Delta t}S_{ij}$) and the Green-Lagrange strain tensor (${}_t^{t+\Delta t}\varepsilon_{ij}$) are energetically conjugate, Eq. (4.1.1) can be written as

$$\int_{{}_tV} {}_t^{t+\Delta t}S_{ij}\delta_t^{t+\Delta t}\varepsilon_{ij}d^tV = {}^{t+\Delta t}W, \tag{4.1.4}$$

and as the solution at t is known, we can decompose the unknown strains and stresses

$${}_t^{t+\Delta t}\varepsilon_{ij} = {}_t^t\varepsilon_{ij} + {}_t\varepsilon_{ij} = {}_t\varepsilon_{ij}, \tag{4.1.5}$$

since

$${}_0^t\boldsymbol{\varepsilon} = \frac{1}{2}({}_0^t\boldsymbol{X}^T{}_0^t\boldsymbol{X} - \boldsymbol{I}), \tag{4.1.6}$$

and

$${}_t^{t+\Delta t}S_{ij} = {}_t^tS_{ij} + {}_tS_{ij} = {}^t\sigma_{ij} + {}_tS_{ij}, \tag{4.1.7}$$

since

$${}_t^0\boldsymbol{S} = \frac{{}^0\rho}{{}_t\rho}{}_t^0\boldsymbol{X}{}^t\boldsymbol{\sigma}{}_0^t\boldsymbol{X}^T, \tag{4.1.8}$$

where ${}_0^t\boldsymbol{X}^T$ is the deformation gradient and ${}_t\rho$ is the mass density at t.

The strain increment can be written in terms of linear (${}_te_{ij}$) and nonlinear (${}_t\eta_{ij}$)

Figure 4.1 – Body at $t + \Delta t$ subjected to virtual displacement field given by $\delta \boldsymbol{u}$.

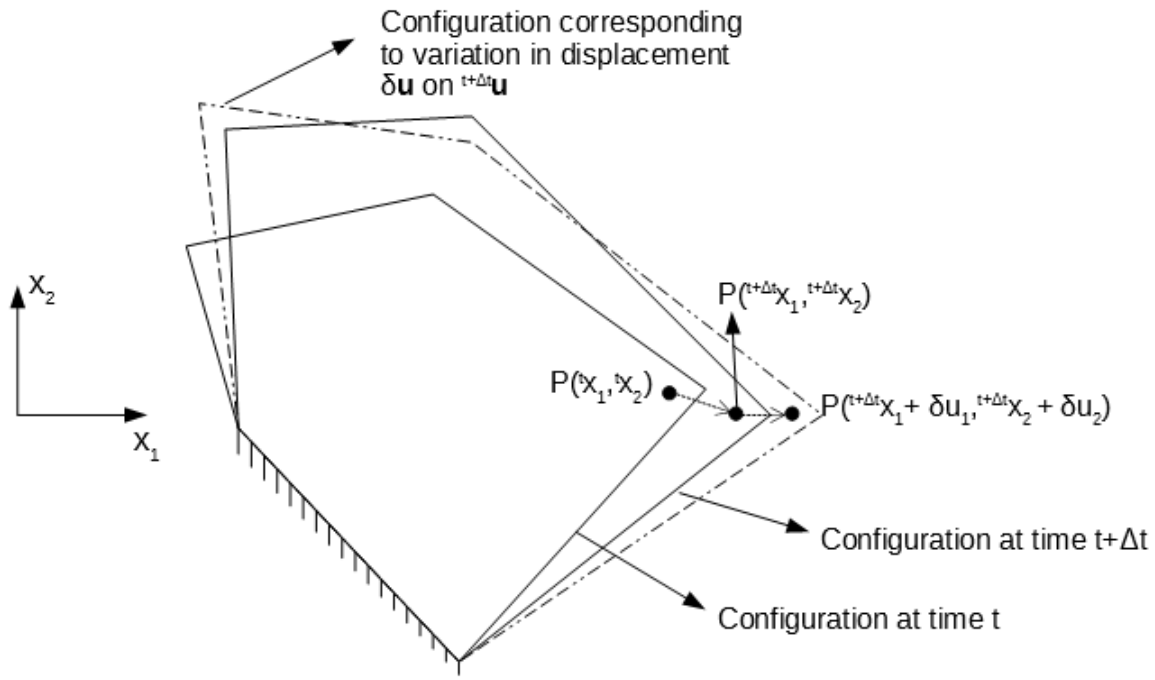

Source: Author's production

contributions

$$ {}_t\varepsilon_{ij} = {}_te_{ij} + {}_t\eta_{ij}, \tag{4.1.9} $$

$$ \delta_t\varepsilon_{ij} = \delta_te_{ij} + \delta_t\eta_{ij}, \tag{4.1.10} $$

where

$$ {}_te_{ij} = \frac{1}{2}\left({}_tu_{i,j} + {}_tu_{j,i}\right), \tag{4.1.11} $$

$$ {}_t\eta_{ij} = \frac{1}{2}{}^tu_{k,i}\ {}_tu_{k,j}, \tag{4.1.12} $$

where the comma denotes differentiation ${}_tu_{i,j} = \dfrac{\partial u_i}{\partial {}^tx_j}$. In this way, Eq. (4.1.4)can be written as

$$ \int_{{}_tV} \left({}^t\sigma_{ij} + {}_tS_{ij}\right)\delta_t\varepsilon_{ij}d^tV = {}^{t+\Delta t}W, \tag{4.1.13} $$

and using Eq. (4.1.10)

$$ \int_{{}_tV} {}_tS_{ij}\delta_t\varepsilon_{ij}d^tV + \int_{{}_tV} {}^t\sigma_{ij}\delta_t\eta_{ij}d^tV = {}^{t+\Delta t}W - \int_{{}_tV} {}^t\sigma_{ij}\delta_te_{ij}d^tV, \tag{4.1.14} $$

where $\int_{{}_tV} {}^t\sigma_{ij}\delta_te_{ij}d^tV$ represents the internal virtual work corresponding to the stresses at t.

Eq. (4.1.14) must be linearised in order to obtain an approximated equation to be solved by the finite element method. To this aim, the second Piola-Kirchhoff stress tensor (${}_tS_{ij}$) can be written as a Taylor series

$$ {}_tS_{ij} = \left.\frac{\partial_t S_{ij}}{\partial_t \varepsilon_{rs}}\right|_t {}_t\varepsilon_{rs} + \text{higher-order terms}, \tag{4.1.15} $$

and by neglecting the higher-order terms,

$$ {}_tS_{ij} = {}_tD_{ijrs}({}_te_{rs} + {}_t\eta_{rs}), \tag{4.1.16} $$

where ${}_tD_{ijrs} = \dfrac{\partial_t S_{ij}}{\partial_t \varepsilon_{rs}}$ is the constitutive tensor referred to the configuration at t. Neglecting nonlinear strain we obtain

$$ {}_tS_{ij} = {}_tD_{ijrst}e_{rs}. \tag{4.1.17} $$

The product ${}_tS_{ij}\delta_t\varepsilon_{ij}$ in the first term of Eq. (4.1.14) can be written as

$$ {}_tS_{ij}\delta_t\varepsilon_{ij} = {}_tD_{ijrst}e_{rs}(\delta_t e_{ij} + \delta_t\eta_{ij}) = {}_tD_{ijrst}e_{rs}\delta_t e_{ij} + {}_tD_{ijrst}e_{rs}\delta_t\eta_{ij}, \tag{4.1.18} $$

where the second term is quadratic in u_i and is neglected, such that

$$ {}_tS_{ij}\delta_t\varepsilon_{ij} = {}_tD_{ijrst}e_{rs}\delta_t e_{ij}. \tag{4.1.19} $$

As ${}^t\sigma_{ij}$ does not depend on u_i and $\delta_t\eta_{ij}$ can be written as

$$ \delta_t\eta_{ij} = \frac{1}{2}{}_tu_{k,i}\ \delta_t u_{k,j} + \frac{1}{2}\delta_t u_{k,i}\ {}_tu_{k,j}, \tag{4.1.20} $$

which is linear in u_i, the second term of Eq. (4.1.14) does not need to be linearised.

Thus the final linearised equation is

$$ \int_{{}_tV} {}_tD_{ijrs}\ {}_te_{rs}\delta_t e_{ij}d^tV + \int_{{}_tV} {}^t\sigma_{ij}\delta_t\eta_{ij}d^tV = {}^{t+\Delta t}W - \int_{{}_tV} {}^t\sigma_{ij}\delta_t e_{ij}d^tV. \tag{4.1.21} $$

Considering thermal effects, ${}_te_{rs}$ can be written as a function of the total strain (${}_te_{rs}^{Total}$) and thermal strain (${}_te_{rs}^{Thermal}$)

$$ {}_te_{rs} = {}_te_{rs}^{Total} - {}_te_{rs}^{Thermal}, \tag{4.1.22} $$

such that Eq. (4.1.21) becomes

$$\int_{{}_tV} {}_tD_{ijrs}\ {}_te_{rs}^{Total}\delta_t e_{ij} d^tV + \int_{{}_tV} {}^t\sigma_{ij}\delta_t\eta_{ij} d^tV = \tag{4.1.23}$$
$${}^{t+\Delta t}W - \int_{{}_tV} {}^t\sigma_{ij}\delta_t e_{ij} d^tV + \int_{{}_tV} {}_tD_{ijrst} e_{rs}^{Thermal}\delta_t e_{ij} d^tV,$$

where the term $\int_{{}_tV} {}_tD_{ijrs}\ {}_te_{rs}^{Thermal}\delta_t e_{ij} d^tV$ represents the internal virtual work corresponding to the thermal loading at t.

4.2 Finite Element Discretization

For the formulation of the finite element equations, the domain V is divided into E finite elements of p nodes and volume V_e. The vector of displacement increments of an element e ,$\Delta\boldsymbol{u}^e$, from t to $t + \Delta T$ can be written as a function of shape functions N as

$$\Delta\boldsymbol{u}^e = \boldsymbol{N}\Delta\boldsymbol{U}^e, \tag{4.2.24}$$

where $\Delta\boldsymbol{U}^e$ is the vector of nodal displacement increments of the element and $\boldsymbol{N}$ is the matrix containing the interpolation functions. The linear strain vector increment ${}_t\boldsymbol{e}$, containing the components of ${}_te_{rs}^{Total}$, can be expressed in terms of the nodal displacement vector $\Delta\boldsymbol{U}^e$ as

$${}_t\boldsymbol{e} = {}_t^t\boldsymbol{B}_L\Delta\boldsymbol{U}^e, \tag{4.2.25}$$

where ${}_t^t\boldsymbol{B}_L$ is the linear strain-displacement transformation matrix.

According to Bathe (1996)

$$\int_{{}_tV} {}^t\sigma_{ij}\delta_t\eta_{ij} d^tV = \delta\boldsymbol{U}^{eT}\left(\int_{{}_tV} {}_t^t\boldsymbol{B}_{NL}^T\,{}^t\boldsymbol{\sigma}\,{}_t^t\boldsymbol{B}_{NL} d^tV\right)\Delta\boldsymbol{U}^e, \tag{4.2.26}$$

where ${}_t^t\boldsymbol{B}_{NL}$ is the nonlinear strain-displacement transformation matrix and ${}^t\boldsymbol{\sigma}$ is the matrix of Cauchy stresses, containing the components of ${}^t\sigma_{ij}$.

In the absence of body and surface forces, substituting Eqs. (4.2.25) and (4.2.26) in Eq. (4.1.24) and assuming that ${}_t\boldsymbol{D}$ is the incremental stress-strain material property matrix, containing the components of ${}_tD_{ijrs}$ and ${}^t\widehat{\boldsymbol{\sigma}}$ is the vector of Cauchy

stresses, containing the components of ${}^{t}\sigma_{ij}$,

$$\delta \boldsymbol{U}^{eT}\left(\int_{{}^{t}V_e} {}^{t}_{t}\boldsymbol{B}^{T}_{Lt}\boldsymbol{D}^{t}_{t}\boldsymbol{B}_{L}d^{t}V\right)\Delta\boldsymbol{U}^{e}+\delta\boldsymbol{U}^{eT}\left(\int_{{}^{t}V_e} {}^{t}_{t}\boldsymbol{B}^{T}_{NL}{}^{t}\boldsymbol{\sigma}^{t}_{t}\boldsymbol{B}_{NL}d^{t}V\right)\Delta\boldsymbol{U}^{e}= \tag{4.2.27}$$
$$-\delta\boldsymbol{U}^{eT}\left(\int_{{}^{t}V_e} {}^{t}_{t}\boldsymbol{B}^{T}_{L}{}^{t}\widehat{\boldsymbol{\sigma}}d^{t}V\right)+\delta\boldsymbol{U}^{eT}\left(\int_{{}^{t}V_e} {}^{t}_{t}\boldsymbol{B}^{T}_{Lt}\boldsymbol{D}_{t}\boldsymbol{e}^{Thermal}\right),$$

where

$${}_{t}\boldsymbol{e}^{Thermal}=\boldsymbol{\alpha}\Delta T \tag{4.2.28}$$

and $\boldsymbol{\alpha}$ is the thermal expansion tensor. After assembling the influence of each element in the finite element mesh, Eq. (4.2.28), we obtain

$$\left(\boldsymbol{K}_{L}+\boldsymbol{K}_{NL}\right)\Delta\boldsymbol{U}=\boldsymbol{F}_{Thermal}-\boldsymbol{F}_{Int}, \tag{4.2.29}$$

where

$$\boldsymbol{K}_{L}=\bigcup_{e=1}^{E}\int_{{}^{t}V_e} {}^{t}_{t}\boldsymbol{B}^{T}_{Lt}\boldsymbol{D}^{t}_{t}\boldsymbol{B}_{L}d^{t}V, \tag{4.2.30}$$

is the linear structural stiffness matrix

$$\boldsymbol{K}_{NL}=\bigcup_{e=1}^{E}\int_{{}^{t}V_e} {}^{t}_{t}\boldsymbol{B}^{T}_{NL}{}^{t}\boldsymbol{\sigma}^{t}_{t}\boldsymbol{B}_{NL}d^{t}V, \tag{4.2.31}$$

is the nonlinear structural stiffness matrix

$$\boldsymbol{F}_{Int}=\bigcup_{e=1}^{E}\int_{{}^{t}V_e} {}^{t}_{t}\boldsymbol{B}^{T}_{L}{}^{t}\widehat{\boldsymbol{\sigma}}d^{t}V, \tag{4.2.32}$$

is the vector of internal forces and

$$\boldsymbol{F}_{Thermal}=\bigcup_{e=1}^{E}\int_{{}^{t}V_e} {}^{t}_{t}\boldsymbol{B}^{T}_{Lt}\boldsymbol{D}\boldsymbol{\alpha}\Delta T d^{t}V. \tag{4.2.33}$$

is the thermal load vector.

As the updated Lagrangian formulation is used, all variables are referred to the last equilibrium configuration t. Thus the total displacement from 0 to $t+\Delta t$ is

$$\boldsymbol{U}^{t+\Delta t}=\boldsymbol{U}^{t}+\Delta\boldsymbol{U}. \tag{4.2.34}$$

The stress increment is

$$\Delta\widehat{\boldsymbol{\sigma}}=\boldsymbol{D}\boldsymbol{e}=\boldsymbol{D}(\boldsymbol{e}^{Total}-\boldsymbol{e}^{Thermal})=\boldsymbol{D}({}^{t}_{t}\boldsymbol{B}_{L}\Delta\boldsymbol{U}-\boldsymbol{\alpha}\Delta T), \tag{4.2.35}$$

such that the total stress at $t + \Delta t$ is

$$\widehat{\boldsymbol{\sigma}}^{t+\Delta t} = \widehat{\boldsymbol{\sigma}}^{t} + \Delta\widehat{\boldsymbol{\sigma}}. \tag{4.2.36}$$

The stress increment, Eq. (4.2.35), depends on the thermal and mechanical strains. As mentioned by Thornton and Dechaumphai (1984), the interpolation of mechanical strain is one order lower than the thermal strain due to the matrix ${}^{t}_{t}\boldsymbol{B}_{L}$, which provides the linear differential of the shape functions, while the term of thermal strain is a direct function of the shape functions $\boldsymbol{N}$. The different order of these terms leads to an unrealistic element thermal stress prediction. Thornton and Dechaumphai (1984) proposed a nodeless parameter approach to reduce the thermal stress discontinuities without adding additional element unknowns. In this approach, the displacement vector is written as

$$\Delta\overline{\boldsymbol{u}}^{e} = \boldsymbol{N}\Delta\boldsymbol{U}^{e} + \overline{\boldsymbol{N}}\Delta\boldsymbol{T}, \tag{4.2.37}$$

where $\Delta\boldsymbol{T}$ is the vector of element nodal temperatures variations and $\overline{\boldsymbol{N}}$ represents the nodeless parameter interpolation matrix (given by Thornton and Dechaumphai (1984))

$$\overline{\boldsymbol{N}} = \begin{bmatrix} \overline{\boldsymbol{N}}_{u1} & \overline{\boldsymbol{N}}_{u2} & \overline{\boldsymbol{N}}_{u3} & \overline{\boldsymbol{N}}_{u4} \\ \overline{\boldsymbol{N}}_{v1} & \overline{\boldsymbol{N}}_{v2} & \overline{\boldsymbol{N}}_{v3} & \overline{\boldsymbol{N}}_{v4} \end{bmatrix}. \tag{4.2.38}$$

For a quadrilateral element, the approximated interpolation functions are

$$\begin{aligned} \overline{\boldsymbol{N}}_{u1} &= \tfrac{\alpha}{16} l_{12}(1-r^2)(1-s); & \overline{\boldsymbol{N}}_{u2} &= -\overline{\boldsymbol{N}}_{u1}; \\ \overline{\boldsymbol{N}}_{u3} &= -\tfrac{\alpha}{16} l_{34}(1-r^2)(1+s); & \overline{\boldsymbol{N}}_{u4} &= -\overline{\boldsymbol{N}}_{u3}; \\ \overline{\boldsymbol{N}}_{v1} &= \tfrac{\alpha}{16} l_{41}(1-r)(1-s^2); & \overline{\boldsymbol{N}}_{v2} &= \tfrac{\alpha}{16} l_{23}(1+r)(1-s^2); \\ \overline{\boldsymbol{N}}_{v3} &= -\overline{\boldsymbol{N}}_{v2}; & \overline{\boldsymbol{N}}_{v4} &= -\overline{\boldsymbol{N}}_{v1}. \end{aligned} \tag{4.2.39}$$

where l_{ij} is the Euclidian distance between nodes i and j and r, s are the local coordinates.

The strain increment, given by Eq. (4.2.25), is rewritten accordingly

$${}_{t}\boldsymbol{e} = {}^{t}_{t}\boldsymbol{B}_{L}\Delta\boldsymbol{U}^{e} + \overline{\boldsymbol{B}}\Delta\boldsymbol{T}, \tag{4.2.40}$$

where $\overline{\boldsymbol{B}}$ is the nodeless parameter strain-displacement matrix. The stress increment than becomes

$$\Delta\widehat{\boldsymbol{\sigma}} = \boldsymbol{D}({}^{t}_{t}\boldsymbol{B}_{L}\Delta\boldsymbol{U} + \overline{\boldsymbol{B}}\Delta\boldsymbol{T} - \boldsymbol{\alpha}\Delta T). \tag{4.2.41}$$

By substituting Eq. (4.2.40) into Eq. (4.1.24), Eq. (4.2.29) becomes

$$\left(\boldsymbol{K}_{L} + \boldsymbol{K}_{NL}\right)\Delta\boldsymbol{U}^{e} = \boldsymbol{F}_{Thermal} - \overline{\boldsymbol{F}}_{Thermal} - \boldsymbol{F}_{Int}, \tag{4.2.42}$$

where

$$\overline{\boldsymbol{F}}_{Thermal} = \bigcup_{e=1}^{E} \int_{V_e} {}^{t}_{t}\boldsymbol{B}_L^T \boldsymbol{D} \overline{\boldsymbol{B}} \Delta \boldsymbol{T} dV \tag{4.2.43}$$

corresponds to the vector associated to the element nodeless parameter interpolation functions.

Chapter 5

Methodology

This work aims at predicting the thermo-mechanical coupling behavior during the SLM process, in order to find the distortions of parts build by this process. The domain, composed by the substrate and powder bed, is subdivided in finite elements. To simulate each added layer, all mesh is generated in the beginning of the process, but the elements of each layer are activated when this new layer is added. Fig. 5.1 shows an example of the activated and deactivated layers and the mechanical boundary conditions.

Figure 5.1 – Example of Activated and deactivated layer.

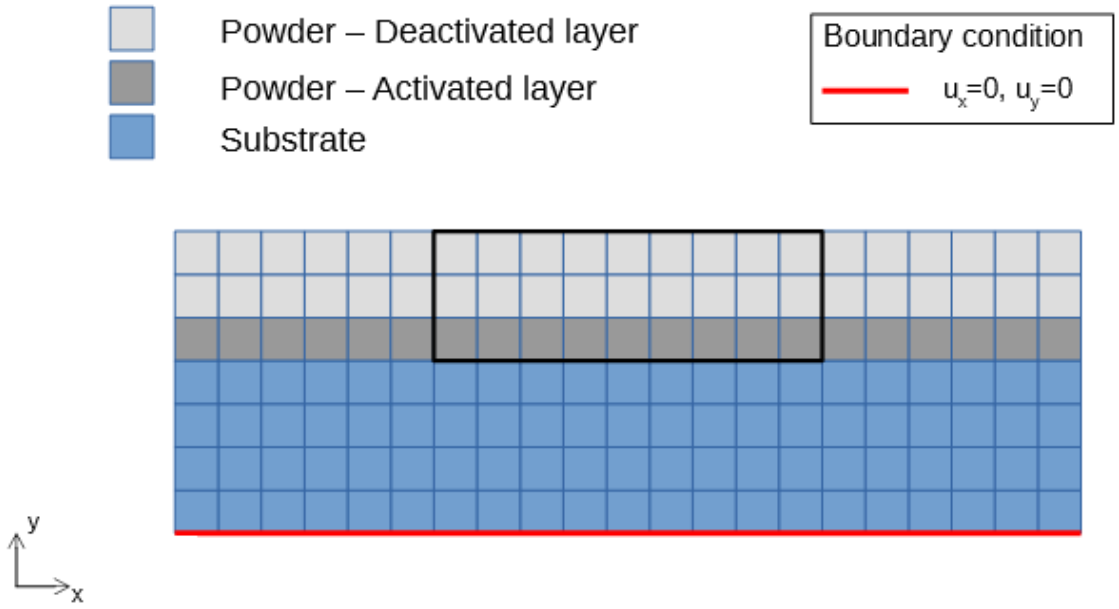

Source: Author's production

The domain is modeled as a two-dimensional problem that is capable of cap-

turing in-plane distortion of the part. In this way, the four node bi-linear isoparametric element is used. The mechanical problem is solved by considering the plane strain assumptions. In the plane strain assumption, the displacement in the z direction is assumed to be zero, as well as it derivatives.

Considering the traditional Saint Venant material model, plane strain hypothesis and an isotropic material we have by definition

$$\varepsilon_{xx} = \frac{\sigma_{xx}}{E} - \nu\frac{\sigma_{yy}}{E} - \nu\frac{\sigma_{zz}}{E} + \varepsilon_{x0}, \tag{5.0.1}$$

$$\varepsilon_{yy} = -\nu\frac{\sigma_{xx}}{E} + \frac{\sigma_{yy}}{E} - \nu\frac{\sigma_{zz}}{E} + \varepsilon_{y0}, \tag{5.0.2}$$

$$\varepsilon_{zz} = -\nu\frac{\sigma_{xx}}{E} - \nu\frac{\sigma_{yy}}{E} + \frac{\sigma_{zz}}{E} + \varepsilon_{z0} = 0, \tag{5.0.3}$$

$$\varepsilon_{xy} = \frac{2(1+\nu)}{E}\sigma_{xy} + \varepsilon_{xy0}. \tag{5.0.4}$$

where ν is the Poisson's ratio and E is the Young's modulus.

In the case of thermal strain

$$\boldsymbol{\varepsilon} = \boldsymbol{D}^{-1}\boldsymbol{\sigma} + \boldsymbol{\varepsilon}_{Thermal}. \tag{5.0.5}$$

Isolating σ_{zz} in Eq. (5.0.3) results in

$$\sigma_{zz} = \nu(\sigma_{xx} + \sigma_{yy}) - E\varepsilon_{z0}, \tag{5.0.6}$$

and substituting Eq. (5.0.6) in Eqs. (5.0.1) and (5.0.2)

$$\varepsilon_{xx} = \underbrace{\frac{\sigma_{xx}}{E}(1-\nu^2) - \frac{\nu\sigma_{yy}}{E}(1+\nu)}_{\text{related to } \boldsymbol{D}^{-1}\boldsymbol{\sigma}} + \underbrace{\nu\varepsilon_{z0} + \varepsilon_{x0}}_{\text{related to } \boldsymbol{\varepsilon}_{Thermal}}, \tag{5.0.7}$$

$$\varepsilon_{yy} = \underbrace{\frac{\sigma_{yy}}{E}(1-\nu^2) - \frac{\nu\sigma_{xx}}{E}(1+\nu)}_{\text{related to } \boldsymbol{D}^{-1}\boldsymbol{\sigma}} + \underbrace{\nu\varepsilon_{z0} + \varepsilon_{y0}}_{\text{related to } \boldsymbol{\varepsilon}_{Thermal}}. \tag{5.0.8}$$

From Eq. (5.0.4)

$$\varepsilon_{xy} = \underbrace{\frac{2(1+\nu)}{E}\sigma_{xy}}_{\text{related to } \boldsymbol{D}^{-1}\boldsymbol{\sigma}} + \underbrace{\varepsilon_{xy0}}_{\text{related to } \boldsymbol{\varepsilon}_{Thermal}}. \tag{5.0.9}$$

The second term of the Eqs. (5.0.7), (5.0.8) and (5.0.9) gives $\overline{\varepsilon}_{Thermal}$ for the plane strain case

$$\overline{\boldsymbol{\varepsilon}}_{Thermal} = \begin{bmatrix} \varepsilon_{x0} + \nu\varepsilon_{z0} \\ \varepsilon_{y0} + \nu\varepsilon_{z0} \\ \varepsilon_{xy0} \end{bmatrix}. \tag{5.0.10}$$

For an isotropic material

$$\varepsilon_{x0} = \varepsilon_{y0} = \varepsilon_{z0} = \alpha\Delta T, \tag{5.0.11}$$

and

$$\varepsilon_{xy0} = 0, \tag{5.0.12}$$

which leads to the thermal strain vector for the plane strain case

$$\overline{\boldsymbol{\varepsilon}}_{Thermal} = \begin{bmatrix} (1+\nu)\alpha\Delta T \\ (1+\nu)\alpha\Delta T \\ 0 \end{bmatrix} = (1+\nu)\alpha\Delta T \begin{bmatrix} 1 \\ 1 \\ 0 \end{bmatrix}. \tag{5.0.13}$$

In order to find the elasticity matrix ($\mathbf{D}$) for plane strain case, Eq. (5.0.6) is substituted in Eqs. (5.0.1) and (5.0.2),

$$\begin{aligned} \tfrac{E}{1+\nu}\varepsilon_{xx} &= \sigma_{xx}(1-\nu) - \nu\sigma_{yy}, \\ \tfrac{E}{1+\nu}\varepsilon_{yy} &= \sigma_{yy}(1-\nu) - \nu\sigma_{xx} \end{aligned} \tag{5.0.14}$$

and, solving for σ_{xx} and σ_{yy}

$$\begin{aligned} \sigma_{xx} &= \tfrac{E}{(1+\nu)(1-2\nu)}\left[(1-\nu)\varepsilon_{xx} + \nu\varepsilon_{yy}\right], \\ \sigma_{yy} &= \tfrac{E}{(1+\nu)(1-2\nu)}\left[\nu\varepsilon_{xx} + (1-\nu)\varepsilon_{yy}\right]. \end{aligned} \tag{5.0.15}$$

From Eq. (5.0.9) we obtain

$$\sigma_{xy} = \frac{E}{2(1+\nu)}\varepsilon_{xy}, \tag{5.0.16}$$

or, in matrix form

$$\begin{bmatrix} \sigma_{xx} \\ \sigma_{yy} \\ \sigma_{xy} \end{bmatrix} = \mathbf{D} \begin{bmatrix} \varepsilon_{xx} \\ \varepsilon_{yy} \\ \varepsilon_{xy} \end{bmatrix}, \tag{5.0.17}$$

where $\mathbf{D}$ is the elasticity matrix for an isotropic material in plane strain case

$$\mathbf{D} = \frac{E}{(1+\nu)(1-2\nu)} \begin{bmatrix} 1-\nu & \nu & 0 \\ \nu & 1-\nu & 0 \\ 0 & 0 & \dfrac{1-2\nu}{2} \end{bmatrix}. \tag{5.0.18}$$

5.1 Heat Source

Complex mechanisms are involved in the melting pool and modeling this phenomenon could become costly when the aim is to predict global behavior of the part to be manufactured. As shown in Chapter 2.2, the laser beam is usually modeled as a Gaussian distribution, as shown in Eq. (2.2.3). When the laser beam reaches the powder bed, the powder absorbs part of the energy until it reaches the melting temperature. From that point, the energy coming from the laser is absorbed by the mushy region (region where both phases coexist, solid and liquid) until the entire region becomes liquid. In the SLM process, the melting pool reaches temperatures above the melting point and remains at this temperature until the laser leaves the region.

A different approach is proposed in this work, consisting in replace both the laser source and the melting pool by a moving prescribed temperature field, in other words, a moving melting pool. The moving melting pool approach aims to simplify the model in order to perform a global analysis of the part, since it does not take into account the complex phenomena happening in the melting pool, considering that the process parameters shown in 2.6 are matched in order to obtain a stable melting pool.

In this approach the mesh size depends on the process parameters, since the dimensions of the melting pool dictate the size of the elements. Fig. 5.2 shows an example of mesh discretization, where it is assumed that the melting pool depth reaches three powder layers, and there is only one element representing the melting pool. The number of elements to model the melting pool is a parameter that can be modified. Since the premise is that the melting pool is stable, after the laser leaves an element, a complete fusion with the surrounding elements is considered.

The moving melting pool approach has the advantage of being easier to implement, since the flux of the laser do not need to be evaluated in each iteration. Another advantage is the possibility of using larger elements in the mesh, making the simulation less costly. However previous experimental tests are needed to find the temperature and the dimensions of the melting pool for each set of process parameters.

A common procedure to prescribe temperature is to substitute the known nodal point temperatures in the heat flow equilibrium equations and delete the corresponding equations from those to be solved (BATHE, 1996).

Figure 5.2 – Example of mesh discretization for the moving melting pool approach.

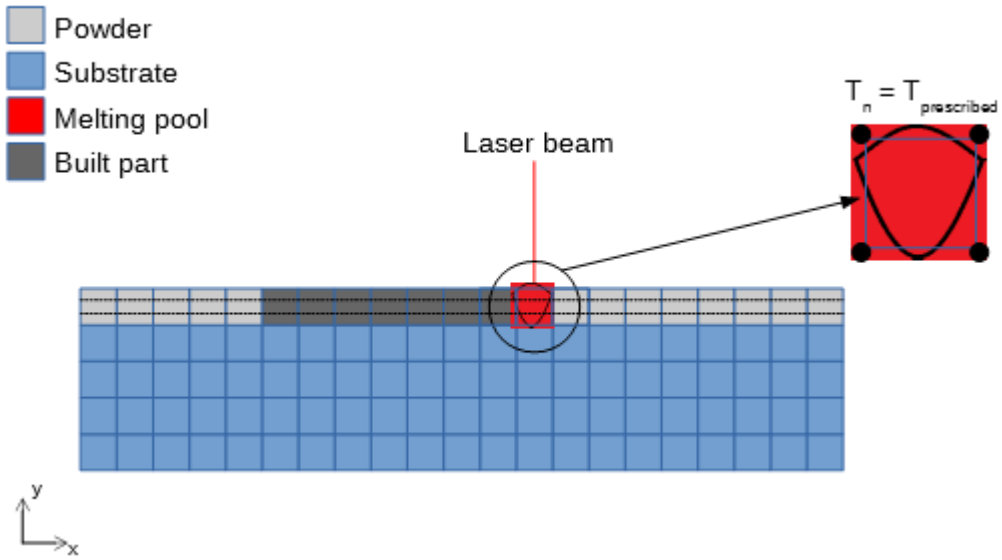

Source: Author's production

5.2 Scanning strategy

The scanning strategy is set by using a list created in the pre-processing phase. As the temperature is prescribed one element at once, the list contains the sequence of the elements that must be molten. For each element, the list gives the number of iterations

$$Ni = \frac{a}{v\Delta t}, \tag{5.2.19}$$

where v is the laser speed, a is the element width and Δt is the time step.

The element number during the part manufacturing (Laser on) is always positive. In this way, the element number is set to -1 when a new layer is added and the laser stays off. The number of iterations that the laser stays off is set to one and a loop is performed until the part and substrate cools down to a given temperature. Another information given by the list is the layer where the laser is. With this information it is possible to check if the layer has changed (such that elements of the new layer must be activated). Fig. 5.3 shows an example of the table of elements.

Figure 5.3 – Table of elements

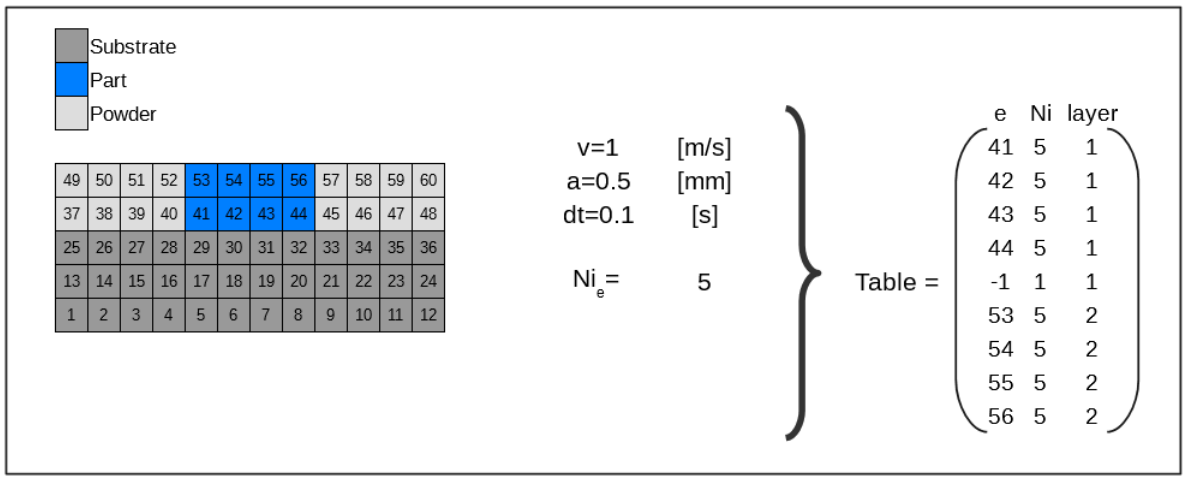

Source: Author's production

5.3 Material Modeling

To describe the material phase of each element during the simulation, a phase function Θ is defined. This function can be expressed as

$$\Theta = \begin{cases} 0 & \text{if Powder} \\ 1 & \text{if Dense Solid (Part)} \\ 2 & \text{if Dense Solid (Substrate)} \end{cases} . \tag{5.3.20}$$

The latent heat of fusion is taken into account as explained in Section 3.1, Eq. (3.1.18), but no liquid phase is included in the material phase function. The liquid phase is included inside the dense solid phase with a temperature test in the subroutine that assigns the material property. At the beginning of the process a vector $\boldsymbol{\Theta}$ is created for all elements in the mesh, including the deactivated elements. Elements belonging to the substrate are set to 2 and the remaining elements are set to 0 (powder). At each iteration, a temperature test determines if some powder element e reaches the melting temperature. In the affirmative case, $\Theta_e = 1$.

A titanium alloy Ti-6Al-4V is used in all simulations performed in this work, since it is widely used in the SLM process. Table 5.1 shows the specific heat, thermal conductivity and density as a function of temperature as well as others properties.

Table 5.1 – Material properties for Ti-6Al-4V.

Physical Properties	Value
Solid Specific Heat $[J/KgK]$	$\begin{cases} 483.04 + 0.2015T & \text{if } T \leq 1268[K] \\ 412.7 + 0.1801T & \text{if } 1268 < T \leq 1923[K] \end{cases}$
Liquid Specific Heat $[J/KgK]$	831
Thermal Conductivity $[W/mK]$	$\begin{cases} 1.2595 + 0.0157T & \text{if } T \leq 1268[K] \\ 3.5127 + 0.0127T & \text{if } 1268 < T \leq 1923[K] \\ -12.752 + 0.024T & \text{if } T > 1923[K] \end{cases}$
Solid Density $[kg/m^3]$	$4420.0 - 0.154(T - 298[K])$
Liquid Density $[kg/m^3]$	$3920.0 - 0.68(T - 1923[K])$
Liquidus temperature $[K]$	1923.0
Solidus temperature $[K]$	1877.0
Evaporation temperature $[K]$	3533.0
Latent heat of fusion $[J/kg]$	2.86 x 10^5
Thermal expansion coefficient $[K^{-1}]$	1.1 x 10^{-5}
Poisson ratio	0.34
Elastic modulus $[GPa]$	107

Source: (MILLS, 2002) and (WELSCH et al., 1993), apud (FAN; LIOU, 2012).

Fig. 5.4 shows that some properties experience large variations over the temperature range of the process. Kolossov et al. (2004) discusses the importance of temperature dependence for the thermal properties. The density of the solid phase is assigned to temperatures smaller than $1877.0[K]$ and the density of the liquid phase is assigned to temperatures larger than $1923.0[K]$. A linear interpolation is used for temperatures between $1877.0[K]$ and $1923.0[K]$ to respect the mass conservation. The modified specific heat in the melting range, obtained with the Apparent Heat Capacity Method is shown in the Fig. 5.5.

Figure 5.4 – Temperature dependent properties.

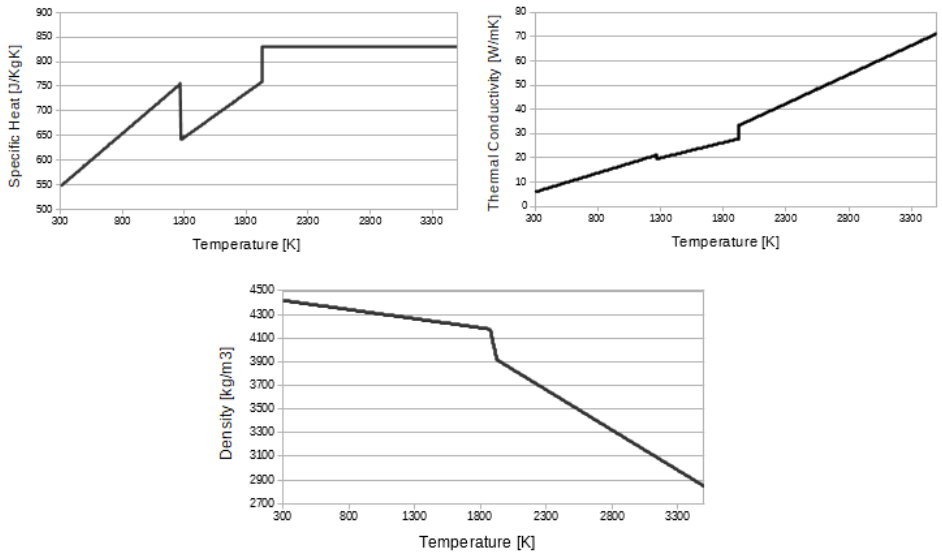

Source: Author's production

Figure 5.5 – Specific heat in the melting region by the Apparent Heat Capacity Method.

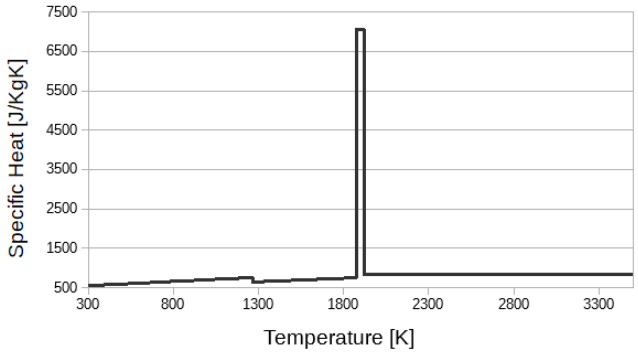

Source: Author's production

Table 5.2 shows the powder properties. The Poisson's ration of the powder is assumed to be zero. The elastic modulus is assumed to be $1.0 \times 10^{-9} E_{solid}$ in order to set a smaller stiffness to that region.

Table 5.2 – Powder properties.

Physical Properties	Value
Specific Heat $[J/KgK]$	6.55 x 10^{-4}
Thermal Conductivity $[W/mK]$	0.2
Density $[kg/m^3]$	2900.0

Source: (KOLOSSOV et al., 2004).

5.4 Mesh Deformation

The thermo-mechanical coupling is performed through Eq. (4.2.33). Taking the initial stress non-linearity into account, the stiffness matrix is add by $\boldsymbol{K}_{NL}$ (Eq. (4.2.31)) and the force vector due to initial stress is also taken into account with $\boldsymbol{F}_{Int}$ (Eq. (4.2.32)). The contribution in force vector due to the nodeless parameter approach is given by $\overline{\boldsymbol{F}}_{Thermal}$ (Eq. (4.2.43)). With the force vector it is possible to find the nodal displacement increments through Eq. (4.2.42). The updated Lagrangian formulation is used, where the coordinates are updated at each time step.

During the SLM process, voids in the powder bed are filled when the powder is melted, causing a densification and decreasing the thickness of the molten powder resulting in shrinkage, as shown in Fig. 5.6-(b) (YU et al., 2016). Fig. 5.6-(a) shows the shrinkage predicted by Yu et al. (2016) during the processing of an AlSi10Mg alloy with $P = 150[W]$ and $v = 400[mm/s]$. To take into account this shrinkage, the top nodes of the molten element are moved downward while respecting mass conservation, as Dai and Shaw (2005). This processis explained in Fig. 5.7.

Figure 5.6 – Shrinkage during the SLM process

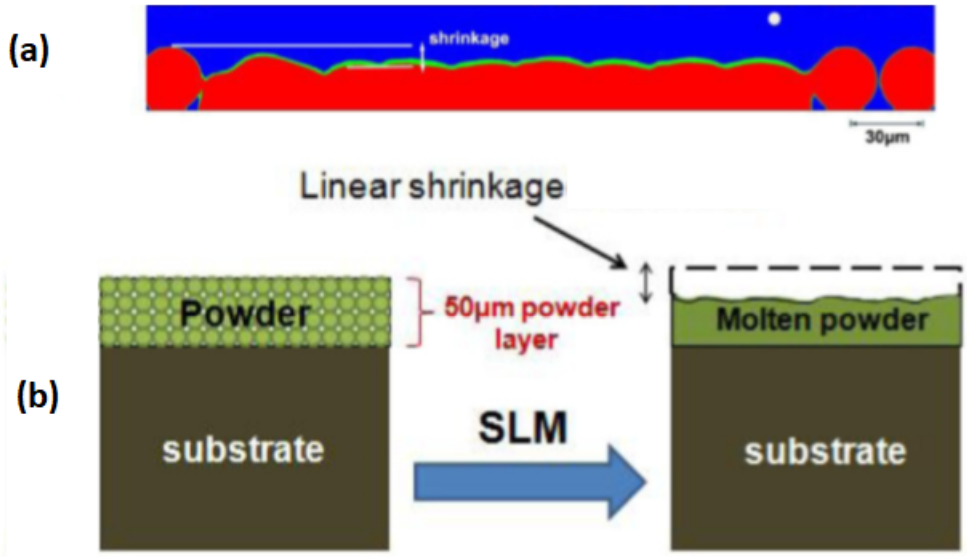

Source: Adapted from (YU et al., 2016).

Figure 5.7 – Shrinkage respecting mass conservation

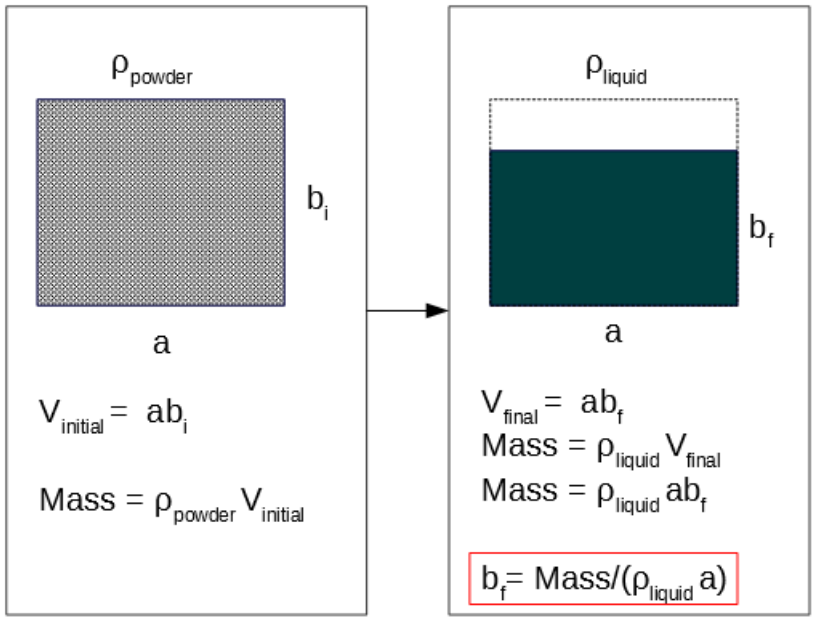

Source: Author's production

5.5 Cooling

Heat transfer mechanisms by conduction and convection are taken into account in this work. The effect of radiation heat losses are neglected (Chapter 2.2).

There are two types of cooling cycles during the process: the cooling before adding a new layer and the final cooling of the part before remove it from the chamber. Two target temperatures can be set in order to take these process parameters into account during the simulation. A new layer is only added when all nodes reach the target temperature. The final cooling is completed when the other target temperature is reached.

5.6 Distortion

After the final cooling, the part is removed from the substrate and the distortion can be calculated. In this work, the vector containing the material phase V_{PHASE} is taken at the end of the process and the informations about the mesh and stresses are considered only in elements belonging to the part. A new problem using residual stresses at the end of the fabrication as initial stresses is then solved considering a new set of boundary conditions. Residual stresses generate internal forces in the form

$$\mathbf{F}_D = -\sum_{e=1}^{E} \int_V \boldsymbol{B}^T \boldsymbol{\sigma} dV, \tag{5.6.21}$$

and the equilibrium equation becomes

$$\boldsymbol{K}_M \boldsymbol{U_D} = \mathbf{F}_D, \tag{5.6.22}$$

where $\boldsymbol{U_D}$ gives the part distortion.

5.7 Flowchart of the Code

The pre-processing produce the mesh and the table of elements (Section 5.2), with dimension Nk, based on the process parameters and laser strategy. A loop is performed into $k \in [1, Nk]$ and an internal loop is performed in $i \in [1, Ni]$. When the counter k is incremented, the layer is checked to verify if a new layer must be added. In the internal loop, the temperature distribution is calculated (Chapter 3) and the value of element e is checked. if $e > 0$ (laser on), nodal temperatures are prescribed (Section 5.1). The nodal coordinates of the molten elements are updated to take the shrinkage into account (Section 5.4). The temperature increment is calculated as well as $\mathbf{F}_{Thermal}$

(Chapter 4). After, displacement and the stresses can be updated (Section 5.4). Fig. 5.8 shows the simulation scheme.

Figure 5.8 – Simulation scheme

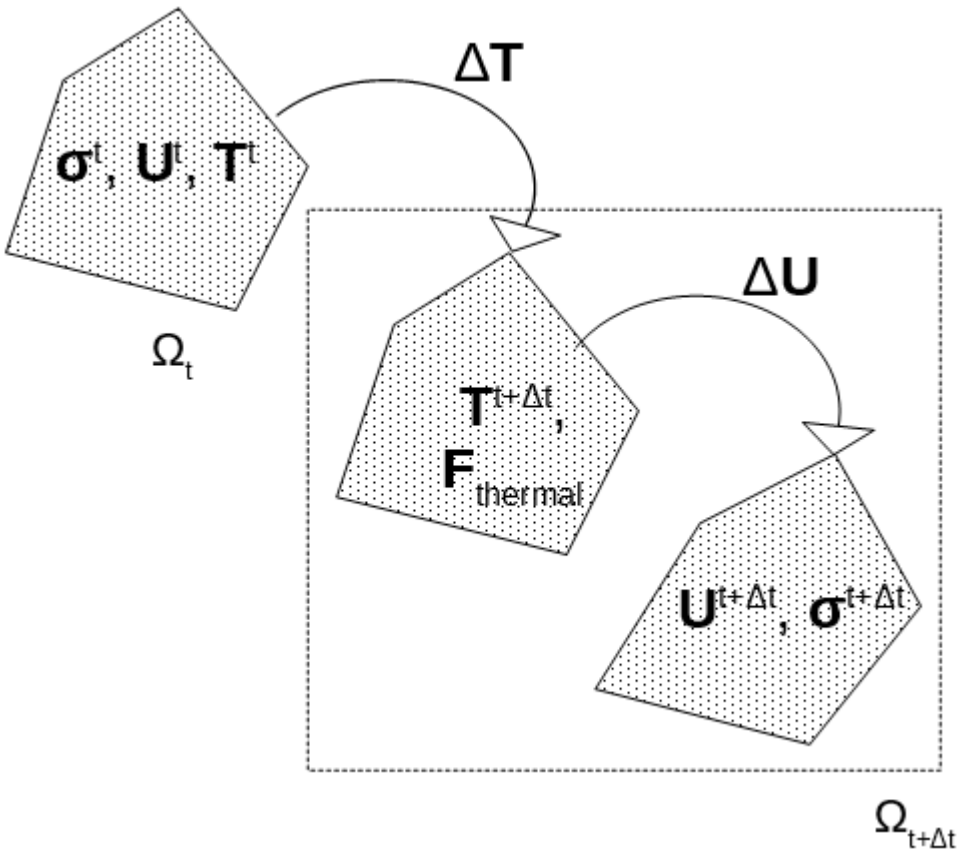

Source: Author's production

At the end of the external loop $k = Nk$ the cooling is started (Fig. 5.9 shows the manufacturing flowchart).

Figure 5.9 – Manufacturing flowchart

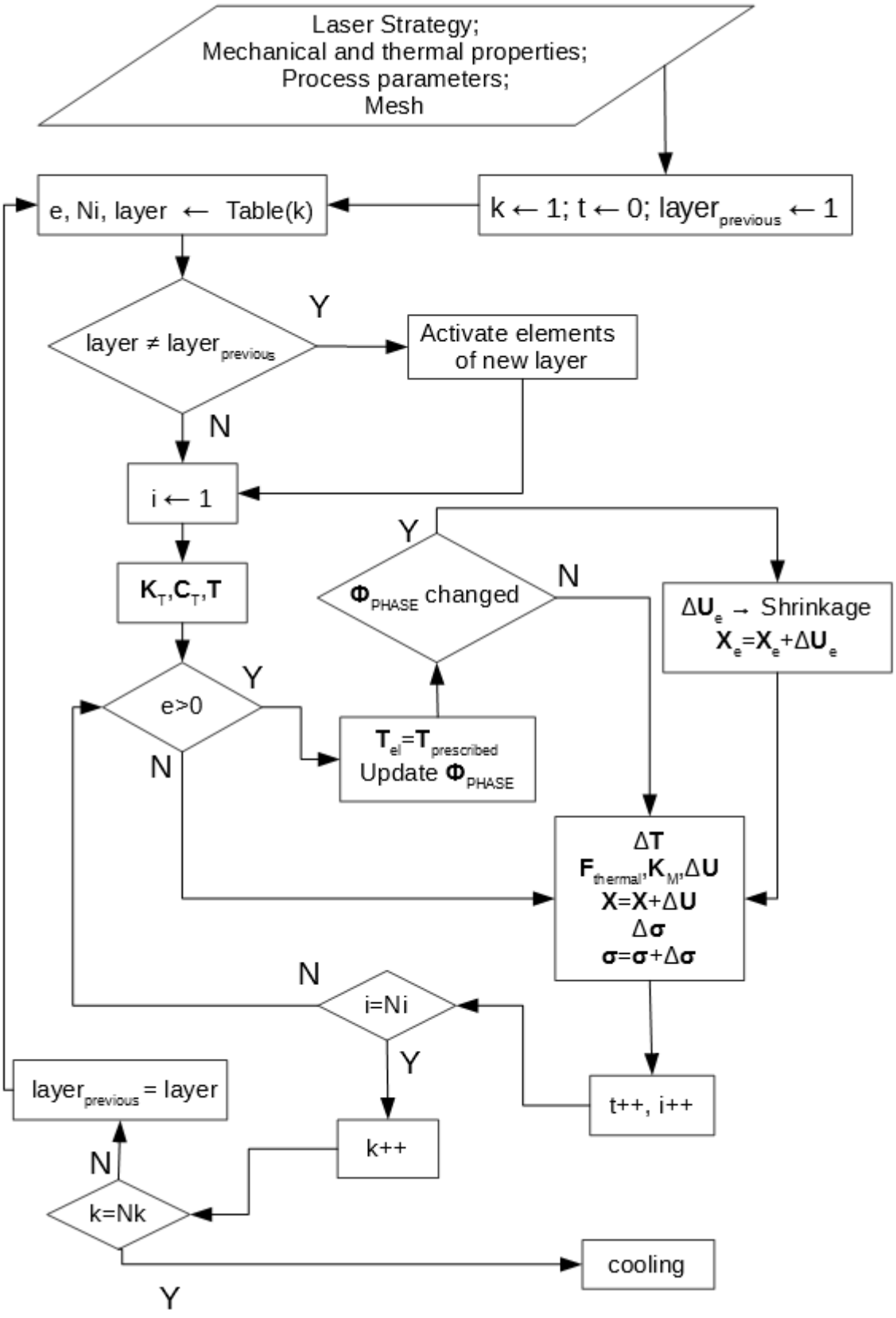

Source: Author's production

In the cooling process, the temperature distribution (Chapter 3), as well displacements and stresses (Chapter 4) are updated until reaching the target temperature. Fig. 5.10 shows the cooling flowchart.

Figure 5.10 – Cooling flowchart

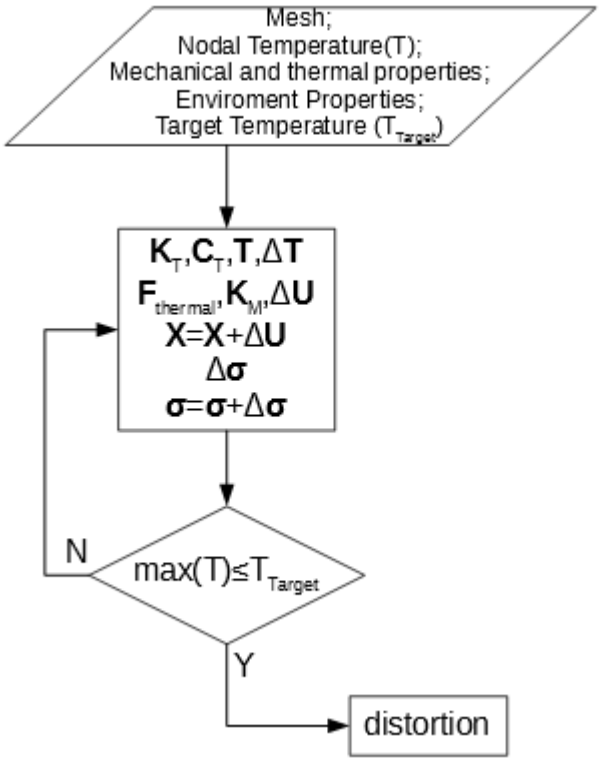

Source: Author's production

The last part consists in evaluating the distortion of the part (Section 5.6), considering the stresses given at the end of the cooling process and the boundary conditions of the problem. Fig. 5.11 shows the distortion flowchart.

Figure 5.11 – Distortion flowchart

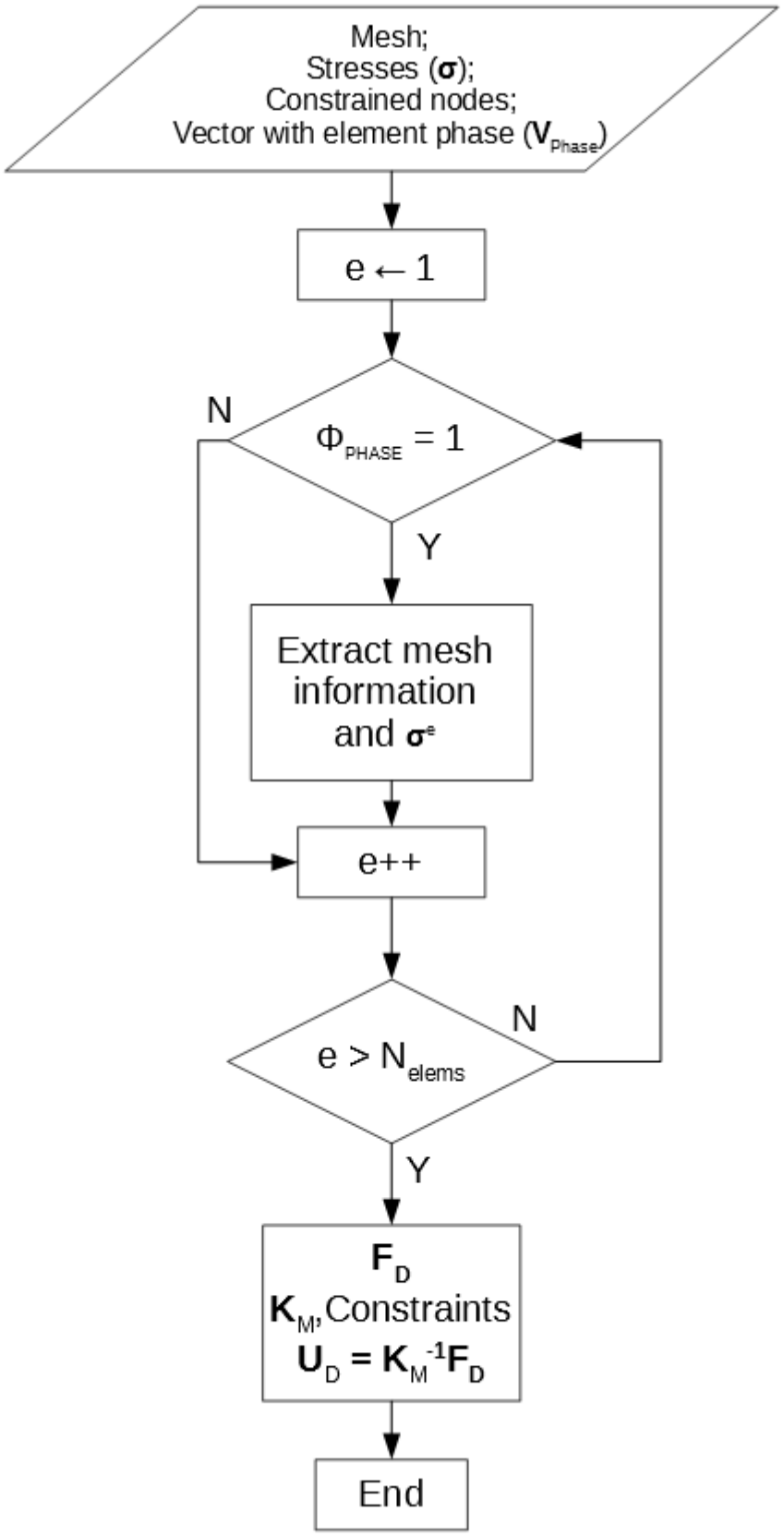

Source: Author's production

Chapter 6

Results and Discussion

This chapter initially describes some process parameters used in most cases analyzed. It is also defined the element size in both the substrate and part as well as the domain to be used. In Section 6.4 it is performed a stability analysis to define the time step to be used in the following simulations. Tested cases as well as the results are presented and discussed in the following sections.

The computer code is written in the free language Julia. The free softwares Gmsh and Gnuplot are used to show temperature distribution and history.

6.1 Process Parameters and Problem description

Some process parameters are taken as default for the simulated cases, as shown in Table 1.1.

Table 6.1 – Process parameters

Laser power (P)	$200[W]$
Scan speed (v)	$0.5[m/s]$
Layer thickness (t)	$20[\mu m]$
Convection coefficient (h)	$20[W/m^2K]$
Ambient temperature (T_a)	$333[K]$
Substrate initial temperature (T_s)	$473[K]$
Target temperature between two layers (T_{Target^1})	$1700[K]$
Target temperature - Final cooling (T_{Target^2})	$1700[K]$

The laser power, scan speed and layer thickness are parameters that directly affect the melting pool dimensions. According to Yang et al. (2016), Ti-6Al-4V alloy and process parameters shown in Table 6.1 lead to a melting poll width around $170[\mu m]$ and depth around $50[\mu m]$. Using the approach presented in section 5.1, the finite element

dimensions of the part and substrate are chosen in order to model the melting pool using only one element with $150[\mu m]$ in x direction and $50[\mu m]$ in y direction, corresponding to three layers. The dimensions of elements used to model the SLM process found in literature are in a wide range of values. Wu et al. (2017) used elements of $0.02mm$ (width) $\times$ $0.02mm$ (length) $\times$ $0.025mm$ (thickness), Li et al. (2015) used elements of $0.05mm$ (width) $\times$ $0.05mm$ (length) $\times$ $0.0375mm$ (thickness) and Nickel et al. (1999) used elements of $1.2mm$ (width) $\times$ $1.25mm$ (length) $\times$ $0.6mm$ (thickness) to model the powder bed.

A convection coefficient of $20[W/m^2K]$ (ROBERTS, 2012) is applied as a boundary condition on the top surface for the thermal problem.

The ambient temperature is prescribed to the powder when a new layer is spread and is also used in Eq. (3.2.39) to define the contribution of the convection to the force vector in the thermal analysis.

The substrate temperature is prescribed at $t = 0$, according Eq. (3.0.10) and is monitored during the simulation in order to guarantee $T(x, y, z = 0, t) \geq T_S \; \forall t$.

In order to decrease simulation time, the part is removed from the substrate before reaching the ambient temperature. The target cooling temperature before adding a new layer (T_{Target^1}) and to final cooling (T_{Target^2}) is $1700[K]$.

6.2 Test Cases

Seven cases are studied to perform a qualitative analysis about the influence of preheating, laser scan strategy and thermal boundary conditions on the final distortion of the part. These cases are chosen in order to verify the sensibility of the implemented formulation and to compare it with similar results found in the literature. Table 6.2 shows the parameters used in each one of the test cases. Case 5 is considered without preheating (ambient/powder and substrate) and all other cases are considered with $333[K]$ for the preheating of the powder and ambient, varying values of the substrate preheating.

Table 6.2 – Tested cases

Case	Scan Strategy	$T_S[K]$	$T_a[K]$	Thermal Boundary Condition
1	Unidirectional	473	333	$T(x,y,z=0,t) \geq T_S \; \forall t$
2	Unidirectional	333	333	$T(x,y,z=0,t) \geq T_S \; \forall t$
3	Alternating	473	333	$T(x,y,z=0,t) \geq T_S \; \forall t$
4	Alternating	333	333	$T(x,y,z=0,t) \geq T_S \; \forall t$
5	Unidirectional	300	300	$T(x,y,z=0,t) \geq T_S \; \forall t$
6	Unidirectional	523	333	$T(x,y,z=0,t) \geq T_S \; \forall t$
7	Unidirectional	473	333	$T(x,y,z=0,t) = T_S \; \forall t$

Source: Author's production

6.3 Domain Description

Dimensions used in the following simulations are shown in Fig. 6.1, with 40 elements in the length and 14 elements in the height of the substrate and 27 elements in the length and 5 elements in the height of the part, which is equivalent to 12 manufactured layers of $20[\mu m]$ approximately. The dimensions of the part are smaller than real parts manufactured by SLM process in order to minimize the computational effort. This is common in the literature, where Roberts (2012) simulate a part with dimension of $1mm \times 1mm \times 0.15mm$ and substrate with $3mm \times 3mm \times 1mm$, Wu et al. (2017) simulate a part with dimension of $1mm \times 5mm \times 0.075mm$ and substrate with $1mm \times 5mm \times 1mm$ and Li et al. (2015) simulate a part with dimension of $5mm \times 0.6mm \times 0.15mm$ and substrate with $5mm \times 0.6mm \times 5mm$. According to Roberts (2012), it is important to keep a surrounding region from the scanned region to prevent near field effects in the temperature field analysis (he used at least $1mm$). Fig. 6.1 shows the surrounding region used in this work.

Figure 6.1 – Dimensions used to perform the simulations

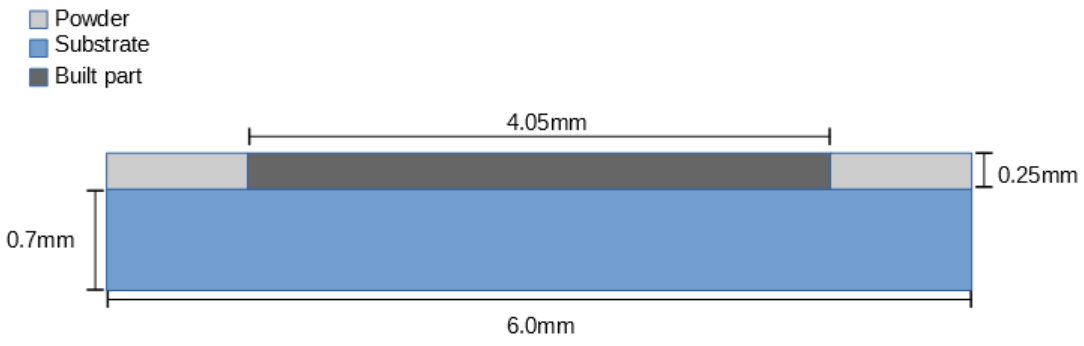

Source: Author's production.

6.4 Stability Analysis

As discussed in Section 3.3, the Finite Difference Method is conditionally stable and the largest Δt for stability is given by Eq. (3.3.41) when the material properties are constant. In the case of temperature dependent thermal properties, this equation does not work and a detailed stability analysis must be performed.

A smaller domain than the one used for the other simulations presented in this work is used in order to decrease elapsed time (Fig. 6.2 (A)). Five time steps were tested to analyze and choose the best value in order to guarantee stability and improve the computational time: $5.0 \times 10^{-10}[s]$, $5.0 \times 10^{-9}[s]$, $1.0 \times 10^{-8}[s]$, $1.2 \times 10^{-8}[s]$, $1.4 \times 10^{-8}[s]$. Six nodes are monitored to verify the stability: 73, 114, 117, 133, 137 and 159, as shown in Fig. 6.2 (B).

Figure 6.2 – (A) Part dimensions used to perform Stability Analysis. (B) Monitored nodes for Stability Analysis

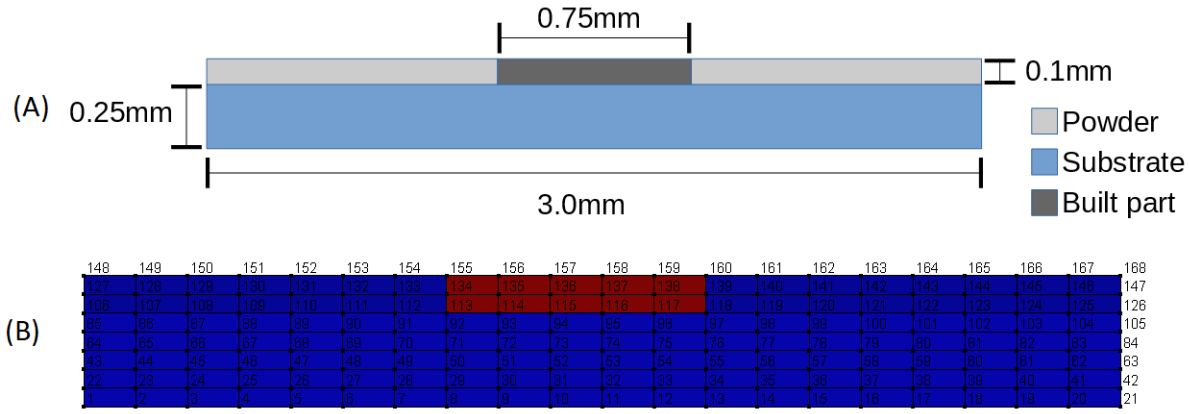

Source: Author's production.

Fig. 6.3 shows the temperature of each node for each time step. The temperature behavior is exactly the same for all time steps at each monitored node, except for $dt = 1.4 \times 10^{-8}$ (purple curve), where the temperature diverges at time $1.5[ms]$ for all nodes.

Fig. 6.4 shows the normalized elapsed time to simulate the part with each time step where it is possible to verify that the simulation time can be drastically reduced using larger time steps.

Thus, the time step, in order to guarantee the stability and also reduce total computation time, is $dt = 1.2 \times 10^{-8}$. This time step is used in all the following simulations.

Figure 6.3 – Temperature of monitored nodes

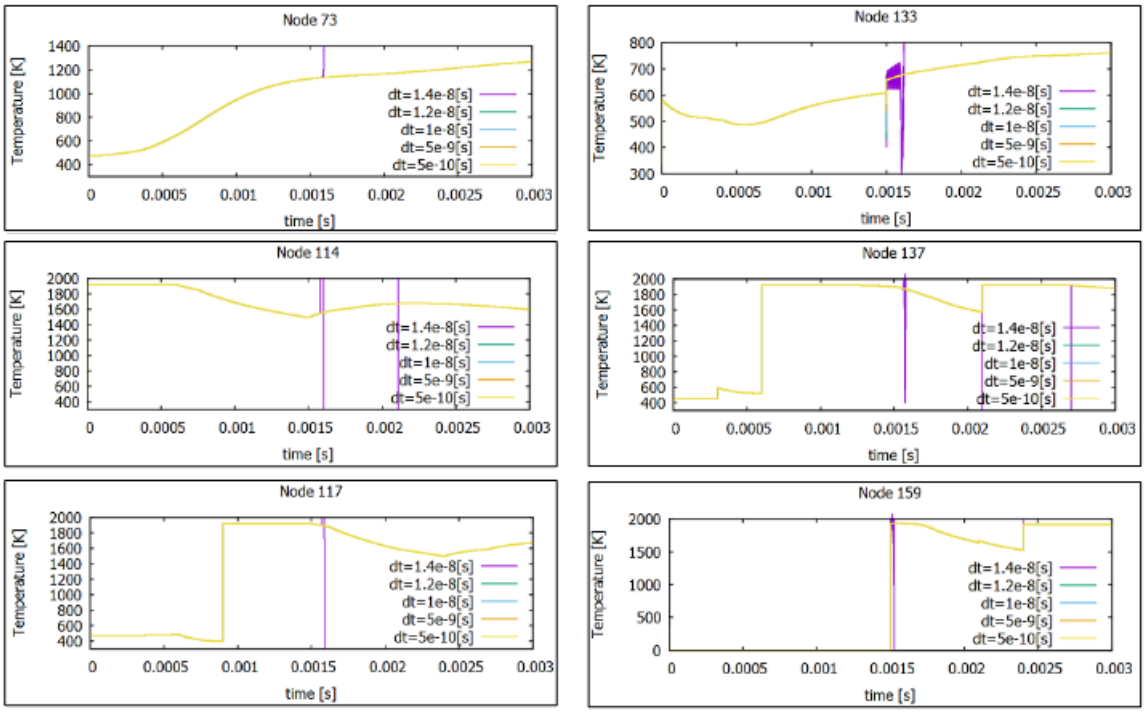

Source: Author's production.

Figure 6.4 – Normalized elapsed time

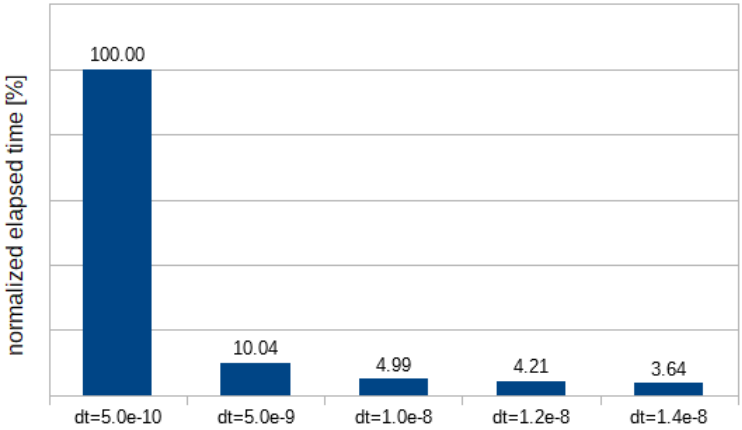

Source: Author's production.

6.5 Thermal Behavior

During the laser scan, Shuai et al. (2013) monitored the temperature of three points along the part depth, spaced by $0.4[mm]$. They concluded that the temperature decreases along the depth (this behavior is presented in Fig. 6.5). It is also possible to note that the cooling cycle takes much longer than the heating cycle.

Figure 6.5 – Temperature history along the thickness obtained by Shuai et al. (2013).

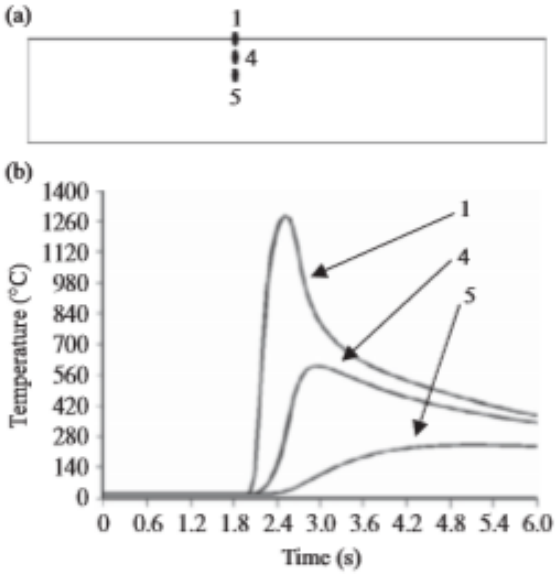

Source: (SHUAI et al., 2013).

In the first simulated case (Tab. 6.2), the temperature of the nodes presented in Fig. 6.6 is monitored during all the manufacturing.

The temperature history of nodes 553, 594 and 635 are shown in Fig 6.7, where it can be seen the same behavior found by Shuai et al. (2013). As the approach used in this work directly apply nodal temperature, simulating the melting pool, the heating rate (around $1.2 \times 10^{11}[K/s]$) is much faster than the heating rate presented by Roberts (2012), that is $2.45 \times 10^{7}[K/s]$. The average cooling rate is around $2.1 \times 10^{5}[K/s]$, within the range of typical cooling rates for laser processing technique (between $10^{3}[K/s]$ and $10^{11}[K/s]$) (ROBERTS, 2012).

Figure 6.6 – Monitored nodes at each time step

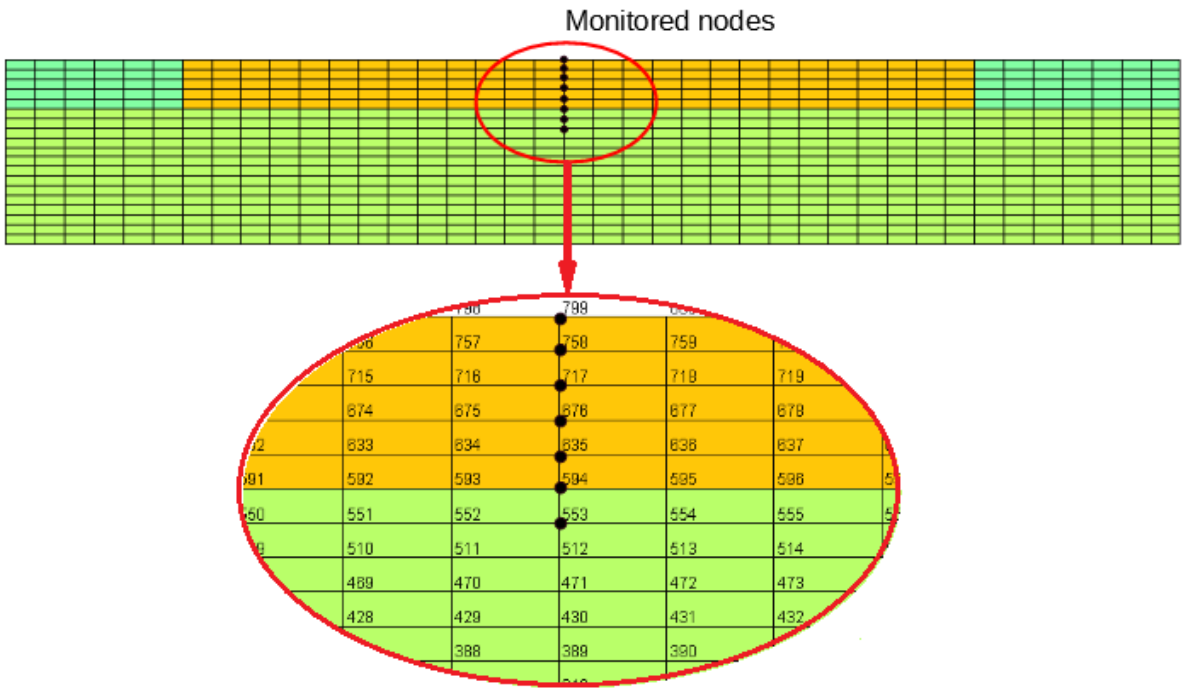

Source: Author's production.

Figure 6.7 – Temperature history of nodes 553, 594 and 635 for case 1 (Table 6.2).

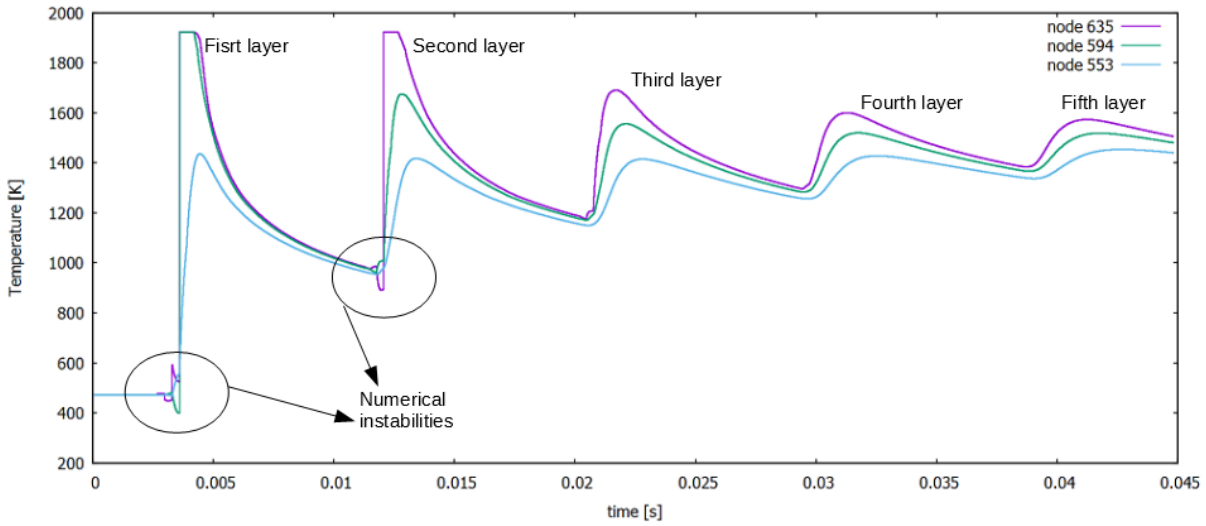

Source: Author's production.

Fig. 6.8 shows the temperature history of nodes 594 and 635 for the scan of the first layer, where it is possible to note that cooling of node 594 is faster than the cooling of node 635. This difference in the cooling rate is associated to the fact that the main heat transfer mechanism is the conduction through the substrate, such that the convection could be neglected, as discussed by Badrossamay and Childs (2007).

Figure 6.8 – Temperature history of nodes 594 and 635 for case 1 (Table 6.2) during the scan of the first layer.

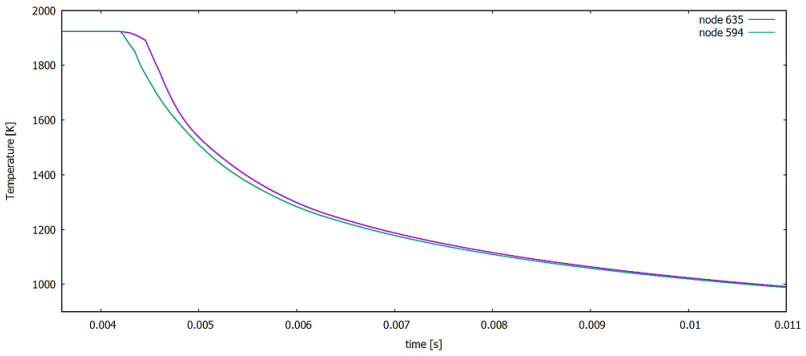

Source: Author's production.

Numerical instabilities shown in Fig. 6.7, where the temperature oscillates before the laser reaches the node, can be solved by using a finer mesh to discretize the melting pool. Case 1 (Table 6.2) is simulated using a finer mesh with element dimensions of $50\mu m \times 50\mu m$ and the difference in the temperature history is shown in Fig. 6.9 for the node 594. It is possible to notice that this instability disappears when a finer mesh is employed. It is also possible to notice a difference in the cooling rate as expected.

Figure 6.9 – Temperature history of node 594 for case 1 (Table 6.2) with element dimensions of $50\mu m \times 50\mu m$ and $150\mu m \times 50\mu m$.

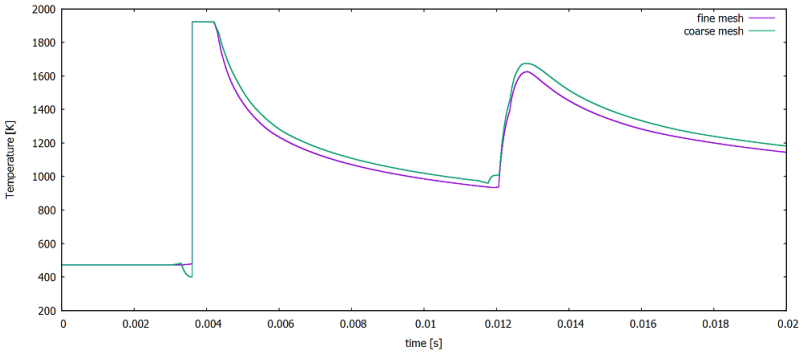

Source: Author's production.

Fig. 6.10 shows temperature field for case 1 (Table 6.2) for both fine and coarse meshes. Global thermal field is the same for both meshes, but it is possible to notice a difference around the melting pool (yellow square), where the nodes do not have the decreasing in temperature before the laser reaches them.

Figure 6.10 – Temperature field for case 1 (Table 6.2) with element dimensions of $50\mu m \times 50\mu m$ (fine mesh) and $150\mu m \times 50\mu m$ (coarse mesh).

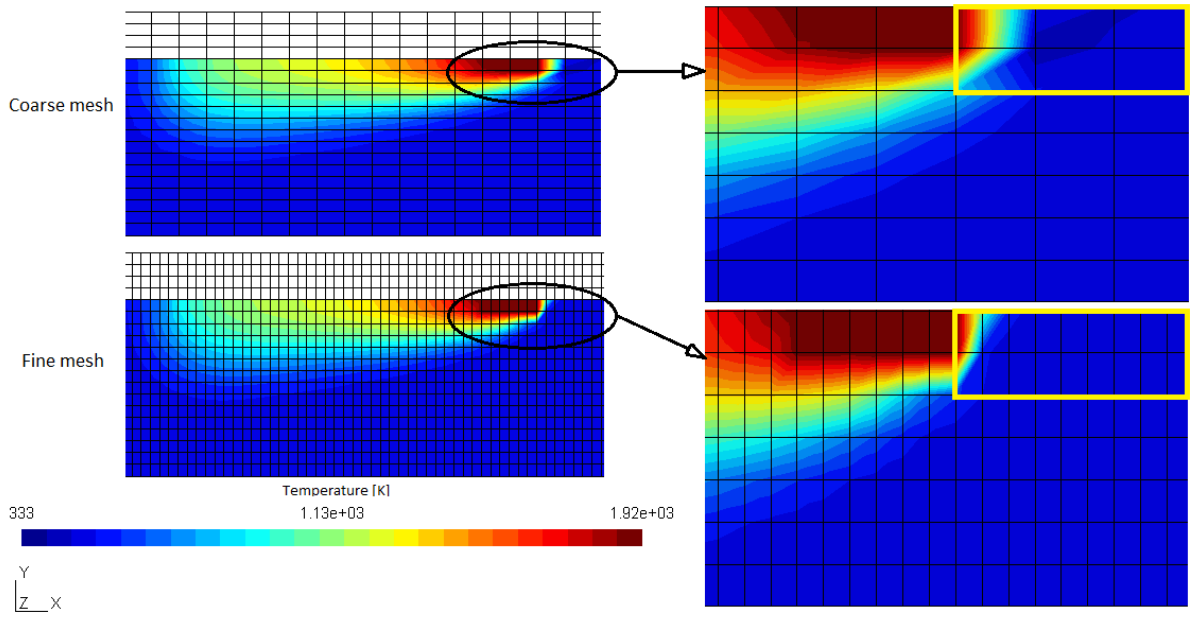

Source: Author's production.

The elapsed time to simulate the problem with a finer mesh is three times larger than the reference mesh. In this way, since the present work proposes a qualitative analysis, and in order to decrease computational efforts, the coarser mesh is employed in the next simulated cases.

6.6 Part Distortion

The final distortion obtained for case 1 (Table 6.2) is shown in Fig. 6.11 as a displacement field. Since the final distortions is evaluated with respect to the initial coordinates, and not with respect to the configuration at the end of the laser scan, nodes 141 to 158 have a negative vertical displacement due the shrinkage applied in the proposed approach.

Figure 6.11 – Displacement field for case 1

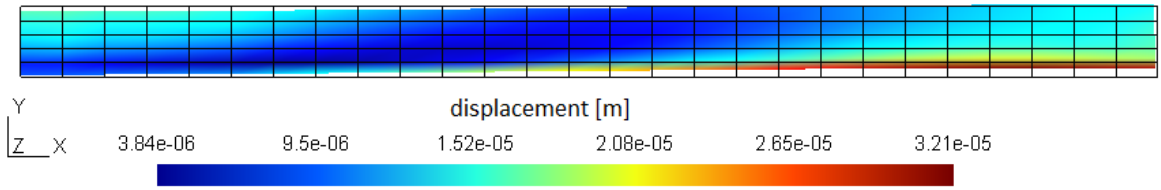

Source: Author's production.

The displacement field displayed in Fig. 6.11 is not easier to analyze. Also, there are many ways to measure and to describe distortion. Thus, in order to make it easer to compare the different cases studied in this work, the final distortion is represented by the vertical displacements of the upper nodes of the part (Fig. 6.12). In the following, the word gain is used whenever some vertical displacement is reduced (less distortion). Fig. 6.12 also shows the nodes (red nodes) held fixed (boundary conditions) to evaluate the distortion.

Figure 6.12 – Vertical displacement u_y (dotted line) of upper nodes is used to represent distortion.

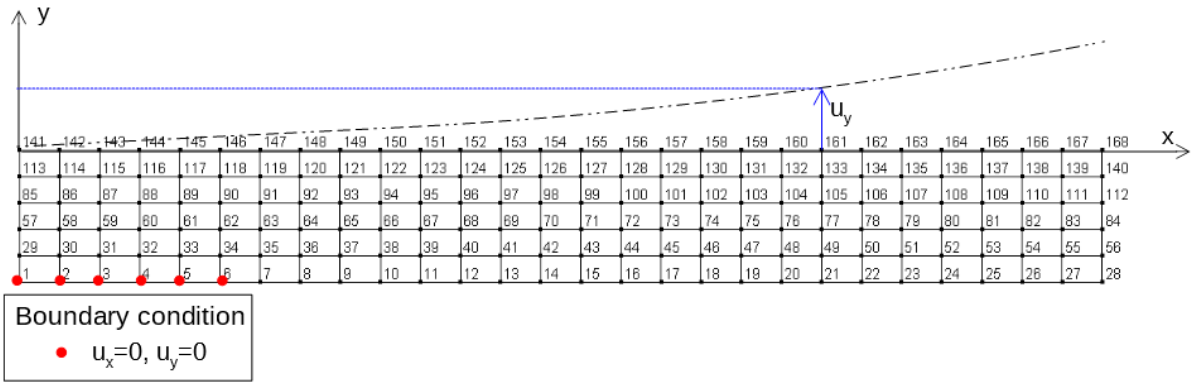

Source: Author's production.

6.7 Scan Strategy

As shown in Section 2.2, the larger the scan vector, larger is the deformation of the part. According to Vrancken (2016), the mechanism behind this effect is not totally clear and can be a combination of several phenomena. Since the present work models

the SLM process as a two-dimensional problem, the comparison of two different scan strategies with larger and shorter scan vectors, like shown in Fig. 2.9, can not be analyzed. However, two different scan strategies are simulated in order to obtain one of the beneficial phenomena cited by Vrancken (2016): a local preheating before scan a new layer. Fig. 6.13 shows the scan strategies used, known as unidirectional and alternating. It is possible to identify that for the alternating strategy, the second layer begin right above the last scanned element, working as a locally preheating.

Figure 6.13 – Unidirectional and Alternating scan strategies

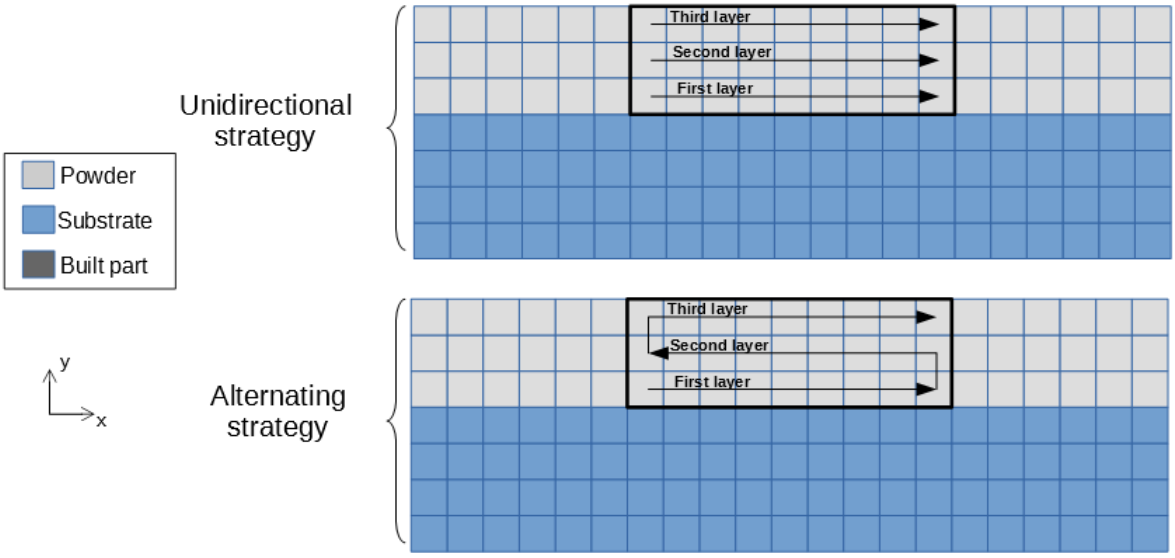

Source: Author's production.

To verify the influence of the scan strategy on the final distortion it is possible to compare the unidirectional and the alternating strategy with $T_S = 473[K]$ (Fig. 6.14) and $T_S = 333[K]$ (Fig. 6.15). For both T_S its possible to identify the same behavior, where the distortion of the part manufactured with an alternating strategy is smaller than the one manufactured with the unidirectional strategy. Comparing the vertical displacement of node 168, in the case of $T_S = 473[K]$, the alternating strategy leads to a displacement 73.50% smaller than unidirectional strategy. In the case of $T_S = 333[K]$, this gain is of 73.97%

Figure 6.14 – Final distortion for unidirectional and alternating strategy with $T_S = 473[K]$.

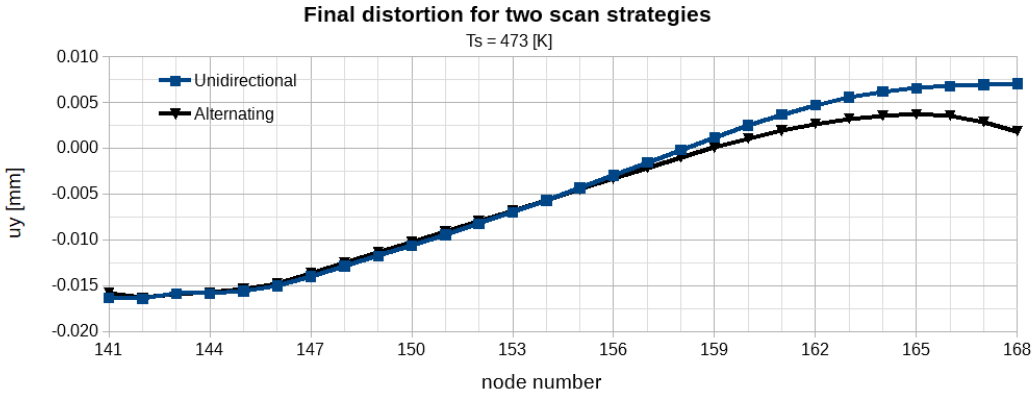

Source: Author's production.

Figure 6.15 – Final distortion for unidirectional and alternating strategy with $T_S = 333[K]$.

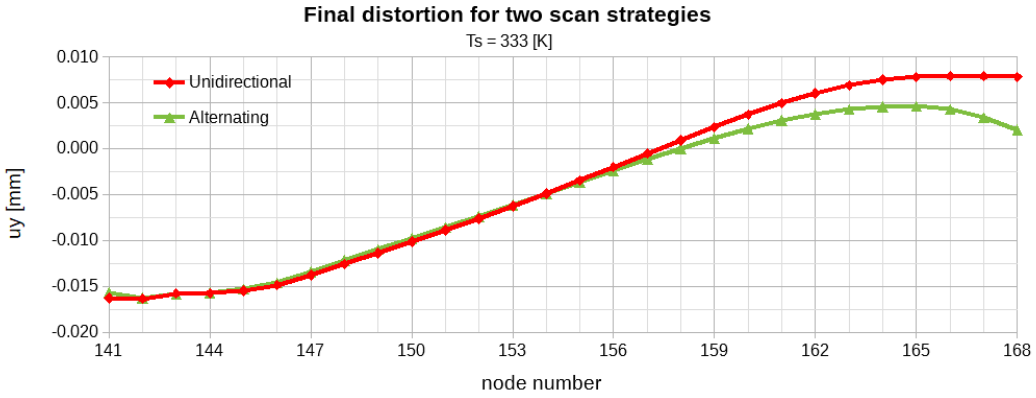

Source: Author's production.

6.8 Preheating

The effect of substrate preheating is analyzed using four different temperatures. The comparison of the extremes temperatures ($300[K]$ and $523[K]$), for the unidirectional strategy is shown in Fig. 6.16, where it is possible to notice that preheating leads to smaller vertical displacements (distortion) of the part.

Figure 6.16 – Final distortion for $T_S = 300[K]$ and $T_S = 523[K]$ with the unidirectional strategy.

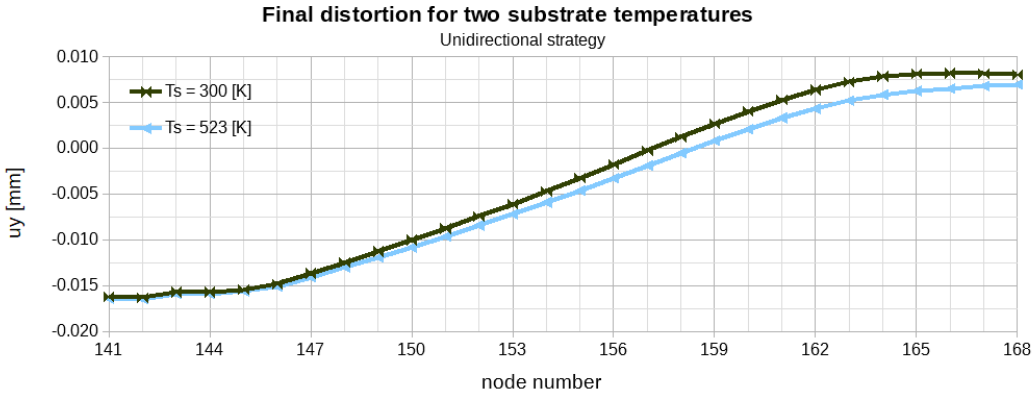

Source: Author's production.

The same behavior is observed when using $T_S = 333[K]$ and $T_S = 473[K]$, for the unidirectional strategy (Fig. 6.17), where the distortion of the part manufactured with $T_S = 473[K]$ is smaller than the one manufactured with $T_S = 333[K]$.

Figure 6.17 – Final distortion for $T_S = 333[K]$ and $T_S = 473[K]$ with the unidirectional strategy.

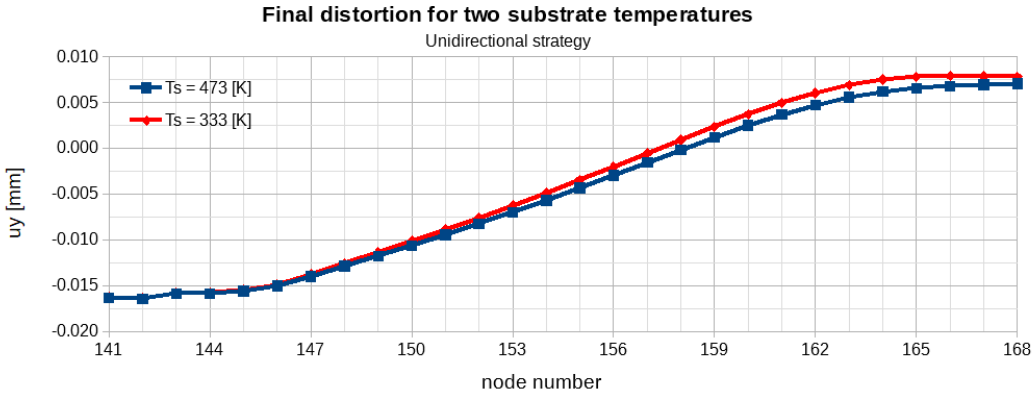

Source: Author's production.

Observing Fig. 6.18, we can conclude that the effect of preheating is beneficial with any scan strategy, since the same behavior is found with unidirectional and alternating strategy.

Figure 6.18 – Final distortion for $T_S = 333[K]$ and $T_S = 473[K]$ with the alternating strategy.

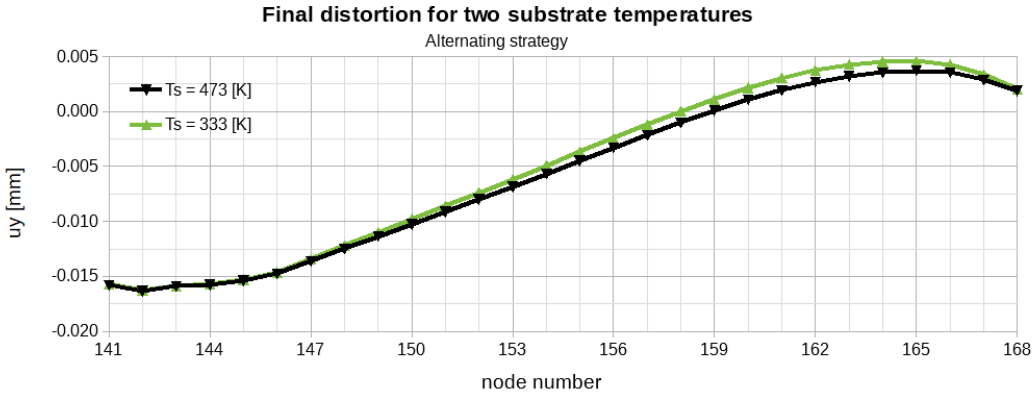

Source: Author's production.

It is possible to notice that the gain obtained with a higher preheating temperature is larger in the vertical displacement of the node 162, as shown in Fig. 6.19.

Figure 6.19 – Zoom of Fig. 6.16 showing the difference in distortion for $T_S = 300[K]$ and $T_S = 523[K]$ with the unidirectional strategy.

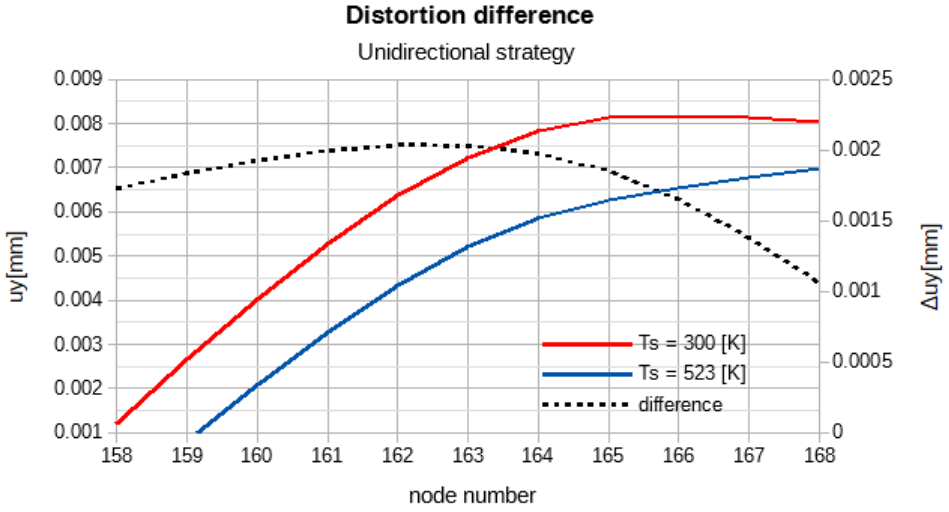

Source: Author's production.

The comparison of vertical displacements of node 162 for all tested preheating temperatures shows a linear relation between the vertical displacement of this node and preheating temperature (Fig. 6.20).

Figure 6.20 – Vertical displacement of node 162 for all tested preheating temperatures

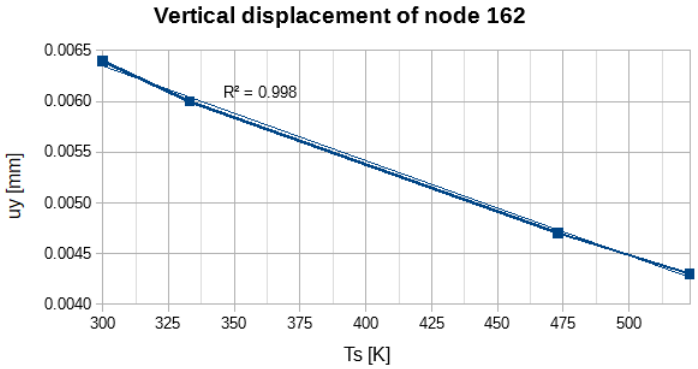

Source: Author's production.

Fig. 6.21 shows the results obtained by Ali et al. (2018), where the difference between the temperature of the top surface of the melting pool and at a point located $250\mu m$ bellow decreases with the increase in the preheating temperature.

Figure 6.21 – Temperature prediction at the top surface of the melting pool and at a point located $250\mu m$ below the melting pool for different preheating temperatures (ALI et al., 2018)

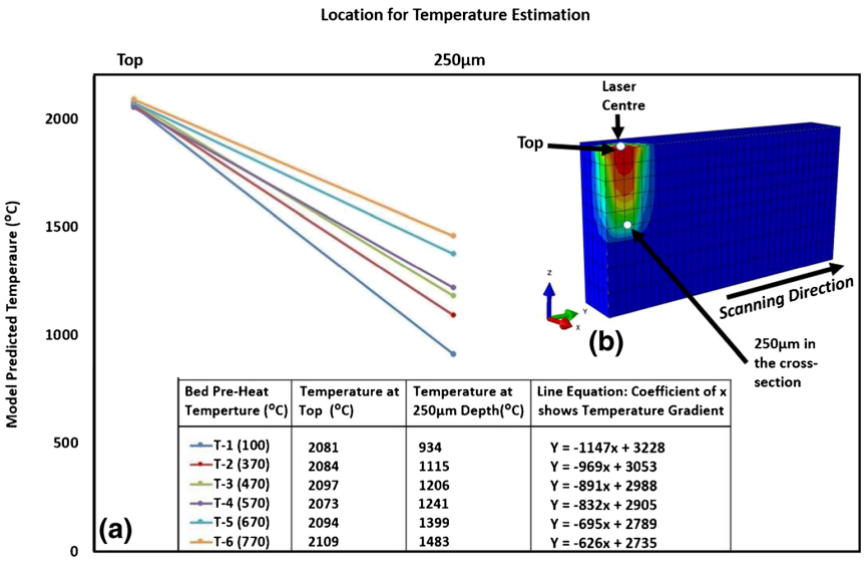

Source: (ALI et al., 2018).

Fig. 6.22 shows the temperature at the top surface of the melting pool and a point located $200\mu m$ below the melting pool for $T_S = 300[K]$ and $T_S = 523[K]$ for the unidirectional strategy. It is possible to notice that the same behavior obtained by

Ali et al. (2018) is achieved, where a higher preheating temperature leads to a lower difference in temperature.

Figure 6.22 – Temperature prediction at the top surface of the melting pool and at a point located $200\mu m$ below the melting pool for $T_S = 300[K]$ and $T_S = 523[K]$ for the unidirectional strategy.

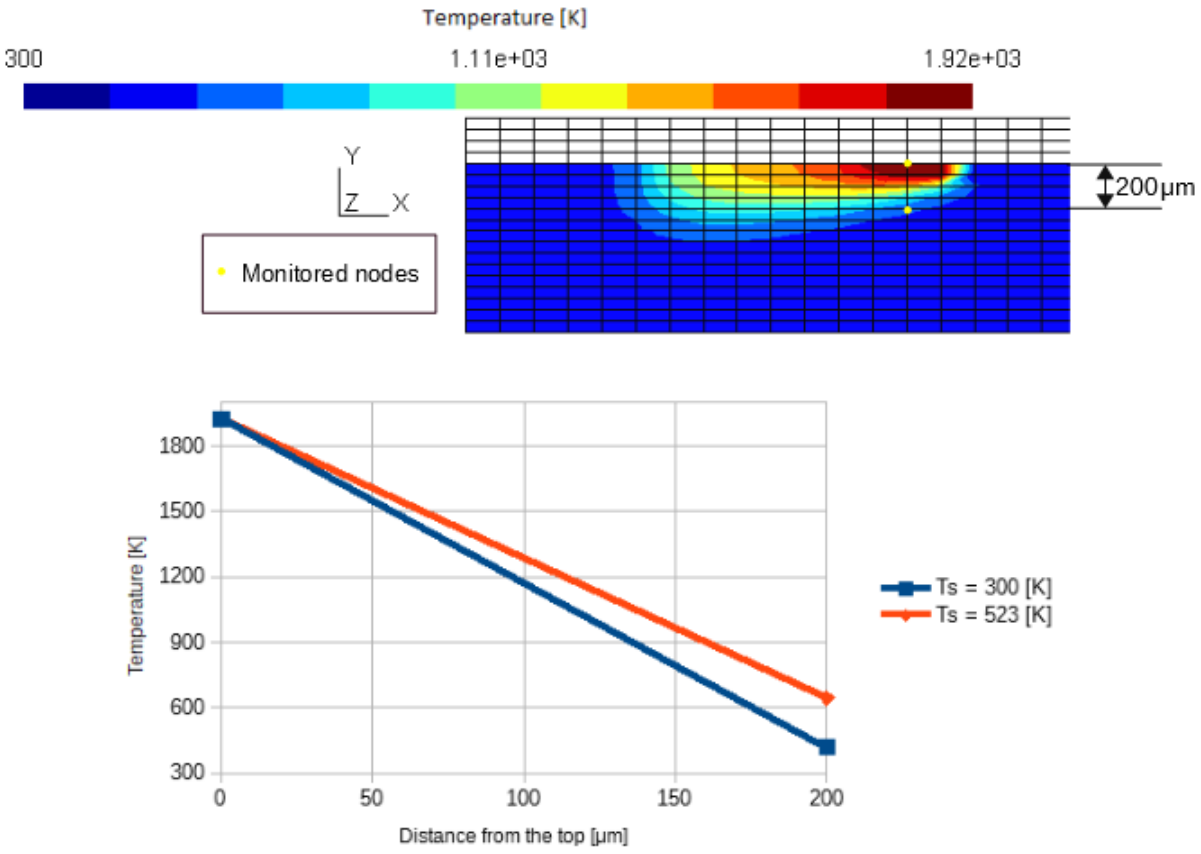

Source: Author's production.

By subtracting the top and the bottom monitored temperatures (Fig. 6.22) and dividing by the distance between the points it is possible to obtain an approximation to the temperature gradient. Doing the same with the results shown in Fig. 6.21, it is possible to notice a linear behavior in the decreasing of the temperature gradient (Fig. 6.23). It is important to notice that the comparison is qualitative, since the parameters used in both simulations are different, as well as the melting pool dimensions.

Fig. 6.24 shows the distortion of a part (shown in the left) for three initial substrate temperatures, where it is possible to notice the beneficial effect of preheating on final distortion. This same qualitative behavior is found in this work, as shown in Figs. 6.16, 6.17 and 6.18, although the effect of preheating seems to be smaller in the proposed formulation.

Figure 6.23 – Comparison of the obtained temperature gradients with the results obtained by Ali et al. (2018) with different substrate preheating.

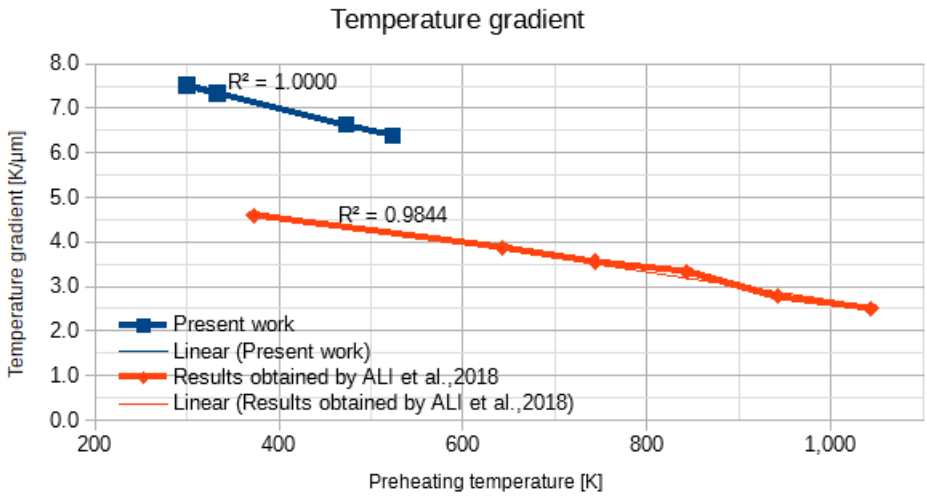

Source: Author's production.

Figure 6.24 – Distortion as a function of initial substrate temperature obtained experimentally by Zaeh and Branner (2010).

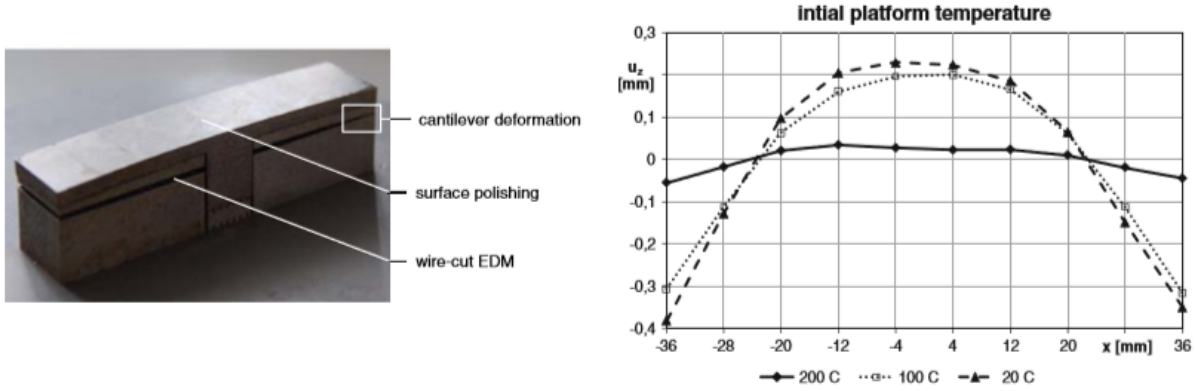

Source: (ZAEH; BRANNER, 2010).

According to Vrancken (2016), the beneficial effect of preheating in residual stress is also given by the decreasing of temperature gradients, since martensitic transformation occurs due to fast cooling rates. However, the most important effect to the reduction of residual stresses is the reduction of the yield stress at higher temperatures. In the present work, mechanical properties are considered to be temperature indepen-

dent and it can explain the low gain in distortion observed when the temperature of preheating is increased.

It is also possible to notice that scan strategy has larger influence on the final distortion than substrate preheating in this work. It is important to emphasize that in the current model, the gain obtained with an alternating strategy is explained by a local preheating and not by a shorter scan vector. In this way, as the local preheating obtained by an alternating strategy is much larger than the preheating assumed as initial substrate temperature, the obtained results are expected.

6.9 Thermal boundary condition

The different kinds of thermal boundary conditions are tested to verify the influence on the final distortion of the part: case 1 ($T(x, y, z = 0, t) \geq T_S$) and case 7 ($T(x, y, z = 0, t) = T_S$). The temperature field during the fabrication of the fourth layer is shown in Fig. 6.25 for both cases, where it is possible to notice that, for the case 1, the substrate can reach temperatures above T_S, since the temperature of the bottom of the substrate is not fixed.

Figure 6.25 – Temperature field during the manufacturing of the fourth layer for case 1 (a) and case 7 (b).

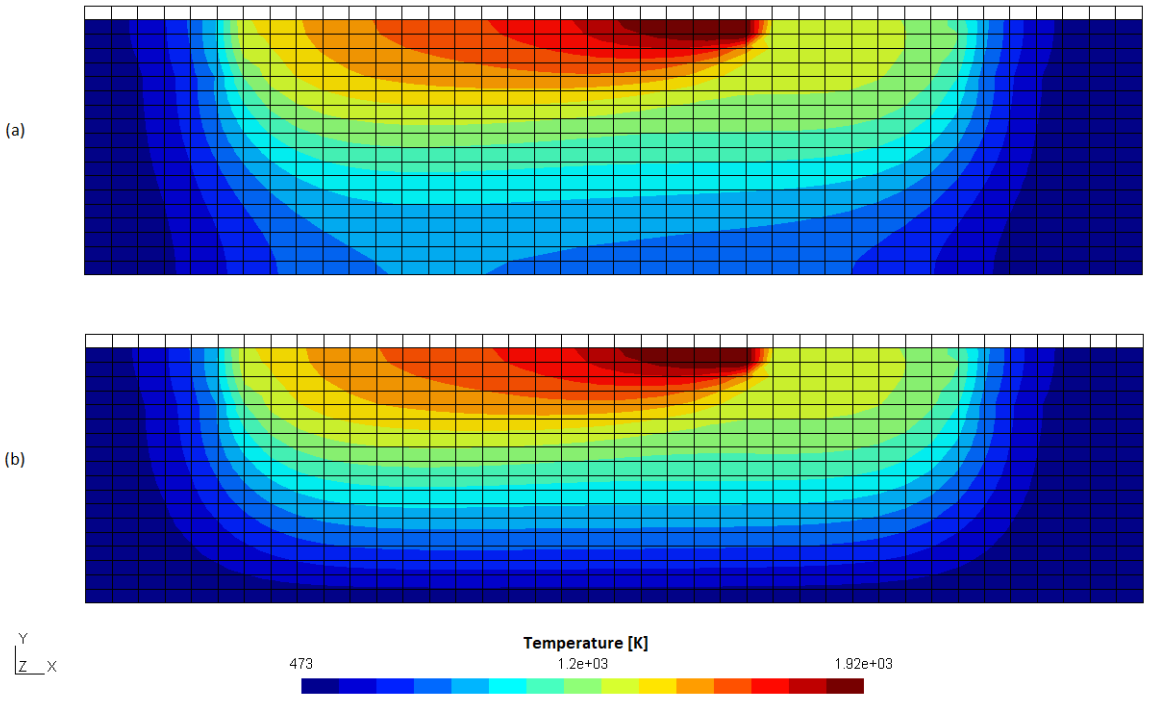

Source: Author's production.

The comparison between the distortion of the final part (Fig. 6.26) for these two thermal boundary condition shows that the distortion of the case 1 is smaller than the case 7. In this way, when the substrate is modeled smaller than the real size (as this work), it is important to remember that this two kinds of thermal boundary conditions can lead to different results.

Figure 6.26 – Final distortion for two different thermal boundary conditions.

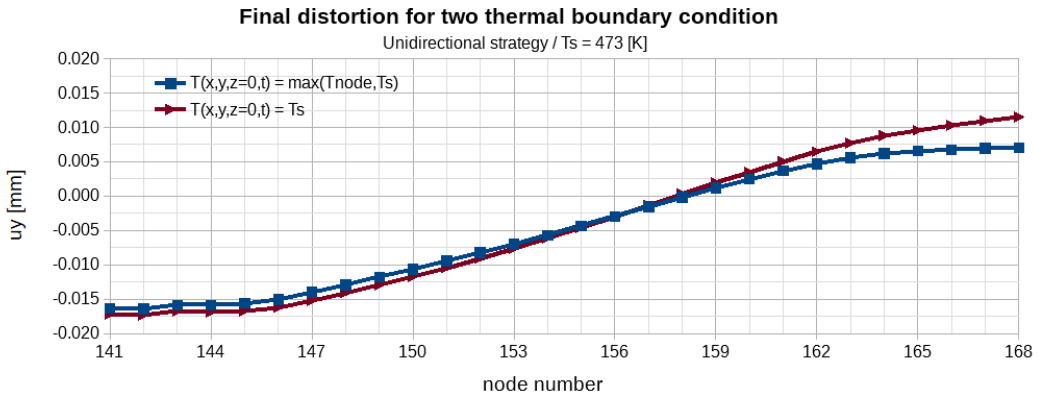

Source: Author's production.

Chapter 7

Conclusions

7.1 Conclusions

In the Selective Laser Melting process, a laser beam selectively scans a powder bed and the energy from the laser is absorbed by the material, leading to a very fast melting. The heat is rapidly conducted through the substrate and the molten material solidifies. These heating and cooling cycles lead to expansion and contraction of the material, but this is constrained by the surrounding solidified material, introducing residual stresses in the part. Residual stresses remaining in the part at the end of the manufacturing can lead to cracks and distortions when the part is removed from the substrate.

Many process parameters can be combined in order to reduce the residual stresses and the final distortion. Preheating of the substrate, in order to decrease the temperature gradient as well as the yield stress of the material, is a good way to decrease the residual stresses, as shown by Vrancken (2016). Short scan vectors are also cited as beneficial to reduce residual stress.

The present work discusses the complex phenomena involved in this manufacturing process and presents a simplified formulation to model the problem. A different kind of laser model is used instead of the Gaussian distribution, where a moving temperature field is used to model the melting pool. A detailed explanation of the formulation and the underlining computer code is presented, in order to be used in future works.

The presented formulation can be qualitatively compared with the literature with a good agreement regarding temperature field, temperature history and final distortion. This shows that the moving melting pool approach can properly model the influence of the melting pool in the global behaviour of the building process.

The analysis of the influence of substrate preheating temperature shows that the gain in the final distortion shall be better modeled by using temperature dependent

mechanical properties.

As the problem is modelled with a 2-Dimensional finite element mesh, there are constraints in scanning strategies that can be used, since different dimensions of scans vector could not be modelled. However, two scan strategies are studied. The alternating scan strategy proved to be beneficial for the final distortion of the part, due to local preheating induced during the scanning with this scan strategy.

The results shown that the proposed formulation is sensitive to both process parameters studied in this work: scan strategy and substrate preheating. In this way, the initial objectives of this research were achieved.

Two different thermal boundary conditions are also studied in this work. This analysis shows that the temperature field is sensitive to this boundary condition as well as the final distortion of the part when the substrate dimensions are modeled smaller than the real size.

7.2 Suggestions for Future Work

In order to improve the results obtained in this work, several aspects are suggested:

- Compare the results obtained by the moving melting pool approach (proposed in this work) with the traditional laser model (Gaussian distribution);
- Perform a sensibility analysis to verify the influence of some parameters as coefficient convection and shrinkage to verify the necessity and influence of these in the simulation;
- Elaborate a formulation to turn the final cooling of the part faster than the traditional formulation in order to decrease computational efforts;
- Implement a 3-Dimensional model;
- Perform experimental tests in order to verify the simulated results;
- Implement thermal-dependent mechanical properties in order to improve the distortion prediction;
- Compare the results obtained with the present time integration formulation (explicit) with an implicit formulation as well the computational effort to verify the viability of the formulation used in this work to simulate larger parts;

Bibliography

ALI, H.; GHADBEIGI, H.; MUMTAZ, K. Residual stress development in selective laser-melted ti6al4v: a parametric thermal modelling approach. *The International Journal of Advanced Manufacturing Technology*, Springer, p. 1–13, 2018.

ALVAREZ, P. et al. Computationally efficient distortion prediction in powder bed fusion additive manufacturing. *Int. J. Eng. Res. Sci*, v. 2, p. 39–46, 2016.

ASTM-INTERNATIONAL. Additive manufacturing - general principles - terminology. *ISO/ASTM Standard 52900*, 2015.

BADROSSAMAY, M.; CHILDS, T. Further studies in selective laser melting of stainless and tool steel powders. *International Journal of Machine Tools and Manufacture*, Elsevier, v. 47, n. 5, p. 779–784, 2007.

BATHE, K.-J. *Finite Element Procedures*. [S.l.: s.n.], 1996.

BREMEN, S.; MEINERS, W.; DIATLOV, A. Selective laser melting. *Laser Technik Journal*, Wiley Online Library, v. 9, n. 2, p. 33–38, 2012.

CALIGNANO, F. et al. Overview on additive manufacturing technologies. *Proceedings of the IEEE*, IEEE, v. 105, n. 4, p. 593–612, 2017.

COOK, R. D.; MALKUS, D. S.; PLESHA, M. E. *Concepts and Applications of Finite Element Analysis*. [S.l.: s.n.], 1989.

DAI, K.; SHAW, L. Finite element analysis of the effect of volume shrinkage during laser densification. *Acta materialia*, Elsevier, v. 53, n. 18, p. 4743–4754, 2005.

ELSEN, M. V. *COMPLEXITY OF SELECTIVE LASER MELTING: a new optimisation approach*. Tese (Dissertation of Doctor in Engineering Science) — CATHOLIC UNIVERSITY OF LEUVEN, 2007.

FAN, Z.; LIOU, F. *Numerical Modeling of the Additive Manufacturing (AM) Processes of Titanium Alloy, Titanium Alloys - Towards Achieving Enhanced Properties for Diversified Applications, Dr. A.K.M. Nurul Amin (Ed.)*. [S.l.]: InTech, 2012.

HUGHES, T. J. *The Finite Element Method Linear Static and Dynamic Finite Element Analysis*. [S.l.]: Prentice Hall, 2000.

IDELSOHN, S. R.; STORTI, M. A.; CRIVELLI, L. A. Numerical methods in phase-change problems. *Archives of Computational Methods in Engineering*, Springer, v. 1, n. 1, p. 49–74, 1994.

KEMPEN, K. *Expanding the materials palette for Selective Laser Melting of metals*. Tese (Dissertation of Doctor in Engineering Science) — Arenberg Doctoral School, 2015.

KEMPEN, K. et al. Lowering thermal gradients in selective laser melting by pre-heating the baseplate. In: *Solid Freeform Fabrication Symposium Proceedings*. [S.l.: s.n.], 2013.

KOLOSSOV, S. et al. 3d fe simulation for temperature evolution in the selective laser sintering process. *International Journal of Machine Tools and Manufacture*, Elsevier, v. 44, n. 2-3, p. 117–123, 2004.

KRUTH, J. et al. *Additive Manufacturing - Innovations, Advances, and Applications:Additive Manufacturing of Metals via Selective Laser Melting Process Aspects and Material Developments*. [S.l.]: CRC Press, 2016.

KUSUMA, C. *The Effect of Laser Power and Scan Speed on Melt Pool Characteristics of Pure Titanium and Ti-6Al-4V alloy for Selective Laser Melting*. Tese (Tesis of Master of Science in Mechanical Engineering) — Wright State University, 2016.

LI, C. et al. Fast prediction and validation of part distortion in selective laser melting. *Procedia Manufacturing*, Elsevier, v. 1, p. 355–365, 2015.

MATSUMOTO, M. et al. Finite element analysis of single layer forming on metallic powder bed in rapid prototyping by selective laser processing. *International Journal of Machine Tools and Manufacture*, Elsevier, v. 42, n. 1, p. 61–67, 2002.

MERCELIS, P.; KRUTH, J.-P. Residual stresses in selective laser sintering and selective laser melting. *Rapid prototyping journal*, Emerald Group Publishing Limited, v. 12, n. 5, p. 254–265, 2006.

MILLS, K. *Recommended Values of Thermophysical Properties for Selected Commercial Alloys*. Woodhead, 2002. ISBN 9781855735699. Disponível em: <https://books.google.com.br/books?id=GaOooR231aAC>.

NICKEL, A.; BARNETT, D.; PRINZ, F. Thermal stresses and deposition patterns in layered manufacturing. *Submitted to Materials Science and Engineering A in March of*, Citeseer, 1999.

ODEN, J. Finite element analysis of nonlinear problems in the dynamical theory of coupled thermoelasticity. *Nuclear Engineering and Design*, Elsevier, v. 10, n. 4, p. 465–475, 1969.

OGOH, W.; GROULX, D. Stefan's problem: Validation of a one-dimensional solid-liquid phase change heat transfer process. In: *Comsol Conference 2010*. [S.l.: s.n.], 2010.

PAL, D.; TENG, C.; STUCKER, B. *Additive Manufacturing - Innovations, Advances, and Applications:Simulation of PowderBased Additive Manufacturing Processes*. [S.l.]: CRC Press, 2016.

RAO, S. S. *The Finite Element Method in Engineering*. [S.l.: s.n.], 2004.

ROBERTS, I. A. *Investigation of residual stresses in the laser melting of metal powders in additive layer manufacturing*. Tese (Thesis of Doctor of Philosophy) — University of Wolverhampton, 2012.

SAUNDERS, M. X marks the spot - find ideal process parameters for your metal am parts. disponivel em: https://www.linkedin.com/pulse/x-marks-spot-find-ideal-process-parameters-your-metal-marc-saunders. acesso em 28/12/2017 as 11:22h. 2017.

SHUAI, C. et al. Simulation of dynamic temperature field during selective laser sintering of ceramic powder. *Mathematical and Computer Modelling of Dynamical Systems*, Taylor & Francis, v. 19, n. 1, p. 1–11, 2013.

SRIVATSAN, T.; MANIGANDAN, K.; SUDARSHAN, T. *Additive Manufacturing - Innovations, Advances, and Applications: Additive Manufacturing of Materials...* [S.l.]: CRC Press, 2016.

STUCKER, B. Additive manufacturing technologies: technology introduction and business implications. In: *Frontiers of Engineering: Reports on Leading-Edge Engineering From the 2011 Symposium, National Academies Press, Washington, DC, Sept*. [S.l.: s.n.], 2012. p. 19–21.

THOMPSON, M. K. et al. Design for additive manufacturing: Trends, opportunities, considerations, and constraints. *CIRP annals*, Elsevier, v. 65, n. 2, p. 737–760, 2016.

THORNTON, E. A.; DECHAUMPHAI, P. *Enhanced Thermal-Structural Analysis by Integrated Finite Elements*. [S.l.], 1984.

VOLLER, V. An overview of numerical methods for solving phase change problems. *Advances in numerical heat transfer*, Taylor & Francis, Washington, v. 1, n. 9, p. 341–380, 1997.

VRANCKEN, B. *Study of Residual Stresses in Selective Laser Melting*. Tese (Dissertation of Doctor in Engineering Science) — Arenberg Doctoral School, 2016.

WELSCH, G.; BOYER, R.; COLLINGS, E. *Materials Properties Handbook: Titanium Alloys*. ASM International, 1993. (Materials properties handbook). ISBN 9780871704818. Disponível em: <https://books.google.com.br/books?id=x3rToHWOcD8C>.

WU, J.; WANG, L.; AN, X. Numerical analysis of residual stress evolution of alsi10mg manufactured by selective laser melting. *Optik-International Journal for Light and Electron Optics*, Elsevier, v. 137, p. 65–78, 2017.

YANG, J. et al. Role of molten pool mode on formability, microstructure and mechanical properties of selective laser melted ti-6al-4v alloy. *Materials & Design*, Elsevier, v. 110, p. 558–570, 2016.

YU, G. et al. On the role of processing parameters in thermal behavior, surface morphology and accuracy during laser 3d printing of aluminum alloy. *Journal of Physics D: Applied Physics*, IOP Publishing, v. 49, n. 13, p. 135501, 2016.

YUAN, P.; GU, D. Molten pool behaviour and its physical mechanism during selective laser melting of tic/alsi10mg nanocomposites: simulation and experiments. *Journal of Physics D: Applied Physics*, IOP Publishing, v. 48, n. 3, p. 035303, 2015.

ZAEH, M. F.; BRANNER, G. Investigations on residual stresses and deformations in selective laser melting. *Production Engineering*, Springer, v. 4, n. 1, p. 35–45, 2010.

ZENG, K. et al. Comparison of 3dsim thermal modelling of selective laser melting using new dynamic meshing method to ansys. *Materials Science and Technology*, Taylor & Francis, v. 31, n. 8, p. 945–956, 2015.